EUROPEAN LABORATORY FOR PARTICLE PHYSICS

CERN-EP / 99-48
12.04.1999

CHARGE AMPLIFICATION AND TRANSFER PROCESSES IN THE GAS ELECTRON MULTIPLIER

S. Bachmann, A. Bressan, L. Ropelewski and F. Sauli
(CERN, Geneva, Switzerland)

A. Sharma
(GSI, Darmstadt, Germany)

D. Mörmann
(Inst. Exp. Kernphysik, Karlsruhe, Germany)

ABSTRACT

We report the results of systematic investigations on the operating properties of detectors based on the gas electron multiplier (GEM). The dependence of gain and charge collection efficiency on the external fields has been studied in a range of values for the hole diameter and pitch. The collection efficiency of ionization electrons into the multiplier, after an initial increase, reaches a plateau extending to higher values of drift field the larger the GEM voltage and its optical transparency. The effective gain, fraction of electrons collected by an electrode following the multiplier, increases almost linearly with the collection field, until entering a steeper parallel plate multiplication regime. The maximum effective gain attainable increases with the reduction in the hole diameter, stabilizing to a constant value at a diameter approximately corresponding to the foil thickness. Charge transfer properties appear to depend only on ratios of fields outside and within the channels, with no interaction between the external fields. With proper design, GEM detectors can be optimized to satisfy a wide range of experimental requirements: fast tracking of minimum ionizing particles, good electron collection with small distortions in high magnetic fields, improved multi-track resolution and strong ion feedback suppression in large volume and time projection chambers.

Corresponding author: fabio.sauli@cern.ch
Submitted to Nuclear Instruments and Methods in Physics Research

1. INTRODUCTION

The recently developed gas electron multiplier (GEM) consists of a thin polymer foil, metal-coated on each side, and perforated by a high density of holes [1]. With suitable potentials applied, it acts as powerful preamplifier for electrons released by ionizing radiation in a gas, transferring most of the multiplied electron charge to a pickup electrode or to another amplifying device. The structure has been the subject of studies aimed at ascertaining its properties in the detection of soft X-rays and charged particles, in the laboratory and in beam conditions [2-10]. Multiple structures optimized for large gains are also being developed in view of photon detection and imaging applications [11-13]. A large number of GEMs of various shapes and geometry has been built in the CERN workshops[1] to the specifications of interested groups, including several hundred of large size (27x25 cm^2 active) for the HERA-B inner tracker, where they are mounted as pre-amplifier for micro-strip plates [14]. Larger area prototypes are in construction for the COMPASS experiment at CERN, and for the forward tracker of CMS.

The present paper collects the results of systematic work directed at understanding in detail the amplification and charge collection properties of GEM detectors as a function of geometry and applied field, and describes various aspects of operation that can be optimized in order to satisfy specific experimental needs. For an overview of the major findings, the impatient reader is referred to the last section of this work.

2. GEM GEOMETRY

All measurements here described have been performed with GEM electrodes of similar design, having equidistant circular holes in parallel offset rows. The polymer used for manufacturing is Kapton[2], 50 μm thick, with 5 μm copper cladding on both sides[3] (some early models made use of 15 μm thick metal). The relevant geometrical parameters are defined in Fig. 1a. Most of the measurements have been made with devices manufactured with a double mask process, the so-called standard GEMs, having the cross section shown schematically in Fig. 1b. The pattern of holes is first engraved by conventional photolithography on the metal on both sides of the foil; the channels are then opened with a Kapton-specific solvent, using the pattern itself as mask. Due to the chemical process employed, dissolving the unprotected polymer from both sides, holes have a double-conical shape with the diameter in the center of the insulator slightly smaller that at the metal surface. We have explored a range of hole diameters between 40 and 140 μm, and a pitch between 90 and 200 μm; to obtain a good manufacturing quality, avoiding potentially dangerous under-etching, the maximum hole diameter is usually limited to about two thirds of the pitch. To prevent charging-up of the walls, the inner diameter should be as close as possible to the outer, a cylindrical shape being the optimum [4]. For some measurements, we have used special devices manufactured with a single mask process, named conical GEMs, and having the cross section shown in Fig. 1c; they have special properties that will be discussed in section 6.

---

[1] Technology developed by A. Gandi and R. De Oliveira, CERN-EST-MT

[2] Tradename of Du Pont Co., Wilmington DE, USA

[3] Novaclad G2200 produced by Sheldahl Inc, Northfield MN, USA

The optical transparency of the GEM mesh, ratio of open to total area, is given by the expression $\tau = \pi D^2 / 2\sqrt{3}P^2$, assuming cylindrical holes of diameter D at distance P. Fig. 2a shows a close view of a GEM electrode with 100 μm holes at 140 μm pitch; the optical transparency is about 0.46. Fig. 2b shows instead a GEM with the same pitch and 50 μm holes (τ=0.12). For most measurements, the so-called standard GEM design was used, with P=140 μm, D=70 μm (t=0.23). As will be discussed later, compared to the optical, the electrical transparency depends on the applied fields, and can be close to unity.

Measurements have been made both with single and double GEM detectors, having as readout electrode a printed circuit board (PCB) with sets of parallel strips. Figs. 3a and b provide a schematic view of the two configurations, and the definitions of parameters. Ionization is produced by radiation in the upper drift region, while the lower space, where amplified electrons are collected by the readout board is named induction region. In the double GEM detector, the gap separating the two multipliers is the transfer region. A mixture of argon and carbon dioxide, in the volume proportions 70/30, was used for most measurements; the drift, transfer and induction gaps were typically 3, 2 and 1 mm thick, respectively.

The detectors were exposed to a uniform beam of soft X-rays from a generator, with a main emission line at 6 or 8 keV, restricting the irradiated area with external collimators if necessary. Depending on the scope of the experiment, we measured the current in all electrodes, or recorded pulse height spectra on groups of strips with charge amplifiers followed by analogue-to-digital converters. For the estimate of the absolute gain, we measured separately the electron signal current on the PCB electrode, I_S, and the counting rate R for the quasi-monochromatic X-ray spectrum; the gain is then evaluated from the expression $M = I_S (enR)^{-1}$, where e and n are the electron charge and number of ion pairs per conversion (~220 for 6 keV). Owing to charge losses in the amplification and transfer processes, to be discussed later, it is more appropriate to call M "effective" gain, the real gain of the GEM structures being generally larger by a field and geometry dependent factor.

The effective gain can also be estimated directly from the pulse height analysis, but is affected in this case from the well known ballistic deficit. We have verified however that, owing to the pure electron collection nature of the signal (without slow ionic components), in the normal range of drift velocities and amplifier time constants, there is only a small effect on the results. Fig. 4 shows a comparison of relative signal amplitudes for soft X-rays as a function of drift field, deduced from a measurement of currents, and from pulse height with two shaping constants (100 ns and 1 μs). The curves essentially coincide, except for very low values of field, due to the small drift velocity and large diffusion. In Fig. 5 we compare the pulse heights recorded using a fast amplifier with 50 ns shaping time [15] for 8 keV X-rays and for minimum ionizing electrons. Because of the spread in time of the collected charge for extended tracks, the minimum value of drift field needed for collection is increased. The apparent increase at high fields for extended tracks is an artifact due to the limited dynamic range of the electronics, saturating on the high end of the Landau energy loss distribution. The result depends of course on the filling gas and drift field values, the difference being smaller for higher values of the drift velocity.

3. ELECTRIC FIELD CALCULATIONS

To study the structure of the electric field in various geometry and conditions we have used two interlaced programs, available at CERN: MAXWELL[4] for field calculations in multi-electrode structures including insulators, and GARFIELD [16] for plotting equi-potential and field lines (actually, electron drift lines). Although the programs are intrinsically three-dimensional, we have for the present study only used simpler two-dimensional projections. The limit of this approach is that, although correctly providing the field structure in the plane containing the holes, it does not represent the behavior along diagonal lines; for example, when estimating the electrical transparency, the regions equidistant from sets of three holes contribute to losses more that the field map along the centers suggest. The charge multiplication properties in the holes are instead qualitatively rather well estimated by an inspection of the field lines in the two-dimensional plots.

Fig. 6 shows the field map of a "standard" GEM with D=70 μm, d=55 μm, P=140 μm, operated at a difference of potential ΔV_{GEM}= 500 V, with drift and induction fields of 2 and, respectively, 6 kVcm^{-1}. As all field lines from the drift volume enter the holes, it could be inferred that the collection efficiency (or transparency) is close to 100%. In reality, diffusion can cause some losses, although the experimental results indicate that they are negligible for drift fields above few hundred Vcm^{-1}.

On approaching the hole, and starting from a critical value of field, electrons begin to multiply in an avalanche, increasing exponentially along the channel. In absence of dispersing effects, electrons and ions in the avalanche remain confined to the central region of the channel, and are fully transmitted through the structure. Experimental results show however that a field-dependent fraction of the electron charge is collected by the bottom GEM electrode, and of the ions by the top one. This indicates the presence of dispersing effects, collisional or photon-mediated, spreading considerably the avalanche within the hole during the development.

Reversing the values of drift and induction fields, in other words turning the figure by 180º, one would deduce from the count of field lines that the drift efficiency is still full, a statement contradicted by measurements in this geometry and value of fields (see later, and also Ref. [4]). This is a consequence of the limitations discussed above. To qualitatively illustrate the effect, we have computed the field map for a high value of drift field and a reduced GEM voltage (Fig. 7). As it can be seen, many field lines from the drift region terminate on the upper GEM electrode, therefore reducing the drift collection efficiency. Note the two singularity points, corresponding to the inversion in sign of the surface field on the upper electrode. Pending a full three-dimensional calculation, a way to obtain indicative values of the transparency would be to compute the lines of zero field on the electrode surface, and to estimate the ratio of areas with positive and negative fields.

Reversing again the role of the two regions, one can see that the structure can be set to be transparent to electrons while blocking a good fraction of ions generated by a second multiplier (another GEM or micro-pattern device). This permits to achieve a substantial reduction of ion feedback into the drift volume, a characteristic that can be exploited for the read-out of high rate time projection chambers (see section 7).

---

[4] MAXWELL, Ansoft Co Pittsburg PA, USA

Using the same programs, we have studied the behavior of a GEM electrode in presence of strong external magnetic fields perpendicular to the drift direction. The conditions used are those considered optimal for each case, taking into account the electron drift properties (see Appendix 1): for the lower value of one Tesla, a convenient, non flammable mixture of argon-carbon dioxide 70-30 and a drift field of 2 $kVcm^{-1}$ (Fig. 8), and for B=4 T a mixture of argon-dimethylether (DME) in the volume proportions 30-70, and at a higher value of drift field (6 $kVcm^{-1}$, Fig. 9). Despite the appearance of field lines connecting the drift region to the lower GEM electrode, as a result of the lateral spread of the avalanche a large fraction of the amplified electrons, actually comparable to the B=0 case, should still be injected into the lower region. The qualitative nature of this result has to be stressed; nevertheless, the plots show that in both cases a good drift efficiency can be obtained, despite the distortion introduced by the Lorentz force. The efficient operation of a GEM detector at 1 T has been verified experimentally, showing no losses in the collected charge [5].

The field strength in the GEM channels depends on geometry, increasing with the reduction of the hole diameter. An estimate of the multiplication factor is in principle possible with the mentioned programs, offering a full three-dimensional simulation of avalanches; the procedure is however very time consuming. Simpler considerations based on the two-dimensional field maps permit to obtain qualitative estimates. Fig. 10 provides the field component computed along a line perpendicular to the electrodes through the center of the holes, for a GEM with 500 V across the electrodes and identical external fields (6 $kVcm^{-1}$) on the left and right side in the drawing respectively. One can see, as expected, that for narrower holes the field increases, and tends to the parallel plate value (500 V over 50 μm). Owing to the exponential dependence of the Townsend coefficient from the field, the proportional gain increases considerably with the hole reduction. As shown by the dashed curve, computed for 100 μm holes and a field on the right side increased to 10 $kVcm^{-1}$, an effect on gain of the external field can be expected, particularly for wide holes.

The field strength along directions perpendicular to the axis of the holes, at different distances from the center, has a peculiar shape with wide, almost uniform regions in the center and a sharp increase on the sides particularly close to the metal-insulator interface (Fig. 11). As in many other micro-pattern devices, the high field on the cathode edges is considered responsible for the onset of breakdown at high voltages, due to the appearance of spontaneous field emission [17].

4. MEASUREMENTS WITH A SINGLE GEM

4.1 Dependence of gain on the multiplying field

The proportional multiplication imparted to electrons by a GEM electrode has been measured in a wide range of gases and conditions. Increasing exponentially with the applied voltage, the effective gain depends on geometry and external fields; Fig. 12 gives an example, deduced from the electron current measured on the signal electrode of a single GEM detector. The absolute values of current, given in nA in the plots, depend of course on the radiation flux, kept constant throughout the measurements. Although the maximum sustainable gain is affected by rate, no saturation effect at high

gains have been found, even at the highest values of flux (above 10^5 $mm^{-2}s^{-1}$), demonstrating the absence of space charge phenomena (see Ref. [18]).

Fig. 13 gives a collection of experimental values of effective gain, deduced from the electron charge collected at the PCB, as a function of hole diameter, all other conditions being equal (points with error bars). The gain increases considerably with decreasing diameter until around 70 μm, and reaches a plateau for lower values. Measuring all currents in the structure, we have estimated the real GEM gain for three diameters (points on the dashed line); it shows no saturation. We understand the behavior as being due to increasing losses of electrons, generated in the avalanches, to the bottom GEM electrode, when the hole diameter is reduced below a value close to the GEM thickness (an aspect ratio of one). Because of the low value of the induction field used in this set of measurements, the effective gain is about 1/3 of the real. At first disappointing, the saturation effect actually helps to relax the tolerance requirements on the hole diameter, a particularly important feature in view of manufacturing large area detectors. The observation also suggests that, although using thicker GEMs the real gain is bound to increase, due to the longer multiplication path available to electrons, there might be no improvement in the effective gain, since saturation will presumably occur at larger hole diameters. This point should however be verified experimentally.

4.2 Effect of the induction field

We have recorded the electron and ion currents in all electrodes of a single GEM structure, as a function of the induction field and in a range of GEM voltages; selected examples are shown in Fig. 14 for two values of the drift field. As already mentioned, the effective gain increases almost linearly with the induction field: the increase in the electron current on the signal electrode, I_S , is compensated by a decrease of the current collected on the bottom GEM electrode, I_B . The sum of the two currents, $I_{TOT} = I_S + I_B$, represents the real GEM gain (dashed line), and increases slightly with E_I, a reflection of the influence on the field in the GEM channels. The positive current sharing between the top GEM, I_T , and the drift electrode I_D depends on the drift field strength.

In the argon-CO_2 70-30 mixture used, parallel plate multiplication begins in the induction region above 8 $kVcm^{-1}$, with a consequent fast increase in gain and the appearance of a (positive) ion current on the bottom GEM electrode, overtaking the electron current. Attractive because of the increased gain, this mode of operation is considered unsafe, as it may allow a discharge in GEM to propagate to the readout electrode. Moreover, signals detected on the anode develop a characteristic ion tail, with the consequent increase in occupancy (Fig. 15).

Measurements of effective gain in different gas mixtures (argon-DME from 90-10 to 50-50) demonstrate the pure electrostatics nature of the dependence of effective gain on induction field, up to the point of parallel plate multiplication, reached of course at different potentials (Fig. 16). In order to obtain a coherent set of curves, the measurement of signal current was made adjusting the GEM voltage for each mixture to obtain equal values of gain in the middle of the range.

The maximum potential difference attainable on GEM under strong X-ray irradiation (10^4 Hz/mm^2) before discharge presents only a small decrease

towards high values of induction field (Fig. 17), consistent with a slight increase of the real gain. This confirms that the discharge is generated by a transition mechanism that depends on the avalanche size, and not by other charge transfer properties, as discussed in [18].

Affecting the collection of charges, the induction field has also an influence on the gain stability under strong irradiation, as shown by Fig. 18. At a rate of 10^4 Hz/mm^2 and effective gain values around 10^3, a low value of E_I results in a 15% upwards gain shift after 30 minutes of irradiation. At high values of E_I, on the other hand, the gain remains constant, suggesting the effect to be a consequence of the deposit of part of the electrons or ions generated at the avalanche maximum on the nearby Kapton surface, only conspicuous for low induction fields.

4.3 Effect of the drift field on charge collection

Measured with a standard GEM at two values of multiplying voltage (300 and 550 V), the curves in Fig. 19 and 20 show the dependence of the currents in all electrodes for an uniform irradiation, as a function of the drift field and for two values of the induction field (2 and 8 kVcm^{-1}). The dashed curve is the total current, sum of the positive ion currents measured on the drift and on the top GEM electrodes. For a given GEM geometry, the extension of the region of efficient electron collection from the drift region depends on the GEM voltage, but is almost independent from the induction field, as shown in Figs. 21a and b. Since the GEM multiplication factor depends on the applied voltage, the curves (deduced from the pulse height measured on the PCB electrode) have been normalized to unity, with the implicit assumption of full transparency in the plateau region. The small rise of the normalized signal current observed at high GEM voltages can be explained as due to an enhancement ofthe multiplying field at high drift field.

The extension of the region of electrical transparency is determined by the geometry, and as expected is wider for larger optical transparency. Figs. 22a and b compare the dependence of the detected signal on the drift field, for three GEMs having increasing optical transparency: 140/50 (τ= 0.12), 90/60 (τ=0.4) and 140/100, (τ= 0.46). In order to explore a wider range of operating voltages, the CO_2 percentage for the second set of measurements has been increased from 30 to 70%. For both GEMs with large optical transparency, the efficient collection region extends almost to 10 kVcm^{-1}; the gain of the GEM with smaller holes is however five times larger (cf. Fig. 13). This is important for the use of detectors in strong magnetic fields, requiring the use of high values of drift field to reduce the Lorentz angle.

The almost constant signal pulse height in a wide range of drift field, the good energy resolution for soft X-rays and the detection efficiency above 99% measured for charged particles, are suggestive of a full collection of charge from the drift region. It should be noted however that the experimental procedures used for the present work do not provide an absolute measurement for the transparency; the development of devices capable of single electron detection may contribute to clarify this point [13].

The fractional ion feedback, defined as the ratio of drift to total currents, increases with the drift field and depends on the GEM voltage, but only little on the induction field, as shown in Fig. 23a and b for two values of the induction field. A more substantial suppression of the ion feedback can be obtained with multiple structures, as it will be discussed in the next section.

5. DOUBLE GEM STRUCTURES

Assembly in cascade of two GEM electrodes at a close distance permits to reach very high gains, and extends the range of tolerated charge before discharges, a performance exploited to achieve detection of minimum ionizing particles in presence of heavily ionizing tracks [18]. With reference to Fig. 3b, we name the gap between the GEMs transfer region. In good approximation, the overall gain of the double structure is a product of the effective gains of the two elements, obtained at similar values of the external fields; an example is reproduced in Fig. 24 [9]. In estimating gains and current sharing, one has to take into account of course that the transfer field for the first GEM is the drift field for the second, therefore constraining the operation. Fig. 25 shows that the effective gain of a double GEM detector is almost invariant from the sharing of the multiplying voltage between the two GEMs, as far as their sum is constant.

We have made systematic measurements of currents in all electrodes of double GEM structures exposed to an uniform flux of X-rays, varying one parameter at a time; only a few representative examples are given here. General conclusions of the study are discussed in section 7. Except when otherwise indicated, the two GEMs were of the standard 140/70 type, with the drift, transfer and induction regions 3, 2 and 1 mm thick respectively. The filling gas was argon-CO_2 70-30. No special precaution were taken to align the holes in the two GEMs, a requirement we believe to be irrelevant because of the electron diffusion in the transfer gap. Indeed, in typical operating conditions, the rms of the electron space diffusion is ~200 μm in two mm of drift, largely obliterating the hole's structure (see Appendix 1).

Since in our setup the X-ray beam enters the detector perpendicular to the electrodes, the currents generated by conversions in the drift region, doubly amplified, overlap with those produced by singly amplified conversions in the transfer gap. The resulting error is however small for the range of gains in the first GEM covered by the present study (above 40); moreover, for a beam entering from the drift side, absorption in the first GEM electrodes helps reducing the spurious currents. A measurement in the pulse mode, that permits discrimination between singly and doubly amplified charges, does not suffer from the effect.

Fig. 26 shows the currents in the six electrodes constituting the structure, recorded as a function of the drift field, and for three choices of GEM voltages having equal sum (850 V), therefore providing roughly the same total gain. Similarly, Figs. 27 and 28 provide the currents as a function of transfer and induction field. In all cases, the algebraic sum of the currents is sensibly close to zero, demonstrating the self-consistency of the measurements. While the currents measured on drift and signal electrodes are solely given by ions and, respectively, by electrons, on other electrodes the measured value can be a composition of the two.

Despite the complication due to the multi-electrode configuration, some features of the single GEM can be identified, such as the almost linear increase of the signal current with the induction field, and the voltage dependence of the drift transparency. The behavior of the current measured on the bottom electrode of the first GEM, I_{B1} , is of particular interest. As seen for example in Fig. 27, it can change sign at some value of fields: we have found that this can lead to a dangerous instabilities of gain under heavy irradiation with some schemes used to power the detector (see Appendix 3).

Combining data measured in a wide range of conditions, general properties of the double structure can be disentangled. Figs. 29a, b and c compare the signal currents for the three GEM voltages varying, one at a time, the drift, transfer and induction fields. The dependence of the signal current from transfer and induction fields is almost invariant with the voltage sharing between the two GEMs, at constant sum; such is not the case of the dependence on the drift field, a consequence of the increase of the collection efficiency in the last gap for higher values of the voltage in GEM2, for fixed induction field. As expected, a longer drift plateau is obtained for a higher GEM1 voltage.

6. CONICAL GEM

As indicated earlier, some measurements have been made with devices manufactured with a single mask process, having holes with single conical shape, and the metal holes on the two sides rather different in diameter (as schematically shown in Fig. 1c). Conical GEMs behave differently when mounted with the narrow or the wide holes towards the drifting electrons. The gain curves are similar, albeit displaced in voltage; however, as expected, the region of transparency extends to higher drift fields when electrons enter from the wide side [5].

We have repeated gain and stability measurements, in the current mode and at high fluxes, with conical GEMs having 140 μm pitch and holes 90 and 60 μm in diameter on the two sides, followed by a PCB as pickup electrode. Setup and experimental procedures were the same as for the previous measurements. Fig. 30 shows the dependence of the currents on electrodes on the drift field, at constant GEM voltage and induction field, for the wide to narrow and, respectively, narrow to wide electron transport direction. In both cases, the (negative) current on the bottom GEM electrode was estimated from the balance of currents; the total current is the sum of the drift and top GEM currents. Comparing with measurements made with standard GEMs, one can discern several peculiarities. In the configuration with narrow holes at the termination side of the avalanche, a large fraction of the electron current is collected by the lower GEM electrode. In the opposite configuration, thanks to the wide holes at the avalanche's end, a large fraction of the electrons reach the collecting electrode even at moderate values of the induction field. The total collected charge, instead, begin to decrease above a drift field of around 3 $kVcm^{-1}$, due to the reduced optical transparency.

Consistently with previous observations [4], the gain stability under irradiation behaves differently for the two configurations. For the wide to narrow arrangement, the increased loss of electrons to the lower GEM electrode is accompanied by a conspicuous shift upwards of the gain, Fig. 31a; with the avalanche ending at the wide side, there is only a negligible change (Fig. 31b). The observations confirm the presumption, already discussed in section 4.2, that the presence and amount of charging up is strictly correlated to the GEM geometry, and to the strength of the induction field.

7. DISCUSSION OF THE RESULTS

A crucial issue for understanding the GEM operation is the electrical transparency of the various electrodes to charges, function of geometry and fields as shown in the previous sections. Particularly useful for the analysis

are the data obtained with the double GEM detector, despite their apparent complexity, since one can use one multiplier as a variable charge injector into the second, considerably extending the dynamic range of the measurements.

The electrical transparency of a multi-electrode structure is deduced from the number of field lines from the drift region intercepted by the grid, compared to the total. For the simple case of a mesh of parallel wires, the problem has been studied by many authors in the course of development of grid ionization or Frish chambers; a useful expression is given in Appendix 2, providing the grid transparency τ as a function of the ratio of fields and of a parameter ρ, proportional to the optical opacity of the grid.

Plots of normalized pulse height as a function of E_D / E_H, where E_H is the computed value of field in the center of the holes, show a clear dependence on the GEM geometry, and are almost invariant with the GEM voltage, see Fig. 32. In our case, the two-dimensional geometry and the variable field in the GEM holes make the analytical model formally inapplicable. Nevertheless, we have attempted to fit the data with the expression provided in the appendix, naively squared to take into account the two-dimensional nature of the GEM grids; the dashed curves in the figure show the result, obtained for several values of the free parameter ρ. Amazingly, the values best approximating the data are rather close to the square roots of the geometrical opacities of the three GEM models.

In all measurements, particularly for the double GEM, currents on electrodes add algebraically, with a cancellation between electron and ion currents, making it hard to determine the real total gain of the structure. Taking into account however the relative values, a reasonable approximation of the total current is provided by the sum of the (positive) currents measured on the drift electrode and on the upper electrodes of the first and of the second GEM: $I_{TOT} \approx I_D + I_{T1} + I_{T2}$. Dividing the signal current by the total, one gets a reasonable independence of the result from the various fields. As an example, Fig. 33 shows the fractional signal current, I_S / I_{TOT}, plotted as a function of the drift field for the three values of gain sharing between the two GEMs. Similarly, Fig. 34 gives the fractional signal measured for constant GEM voltage at two values of the induction field.

Analysis of the transmission of electrons from GEM into the induction region also shows the invariance of the results when plotted as a function of field ratios, Fig. 35. Onset of the parallel plate multiplication, revealed by the fast increase of the signal, appears of course at lower values of the field ratio for a higher voltage on the second GEM. As for the drift field, the fractional electron current is essentially independent of the transfer field, in all the range of GEM gains, as shown in Figs. 36. The results demonstrate the irrelevance of a representation of the charge transfer processes as a function of the ratio of drift to induction (or transfer) fields, attempted by some authors [19].

A second aspect of the transmission of charges through GEM concerns the amount of positive ions fed back in the transfer and drift regions. Fig. 37 gives the dependence on the drift field of the fractional ion current, I_D/I_{TOT}, fed into the drift gap for several GEM voltages, deduced from the previous measurements. In Fig. 38, a magnified view of the ion feedback in the low drift field region is compared with the electron collection efficiency measured with the same setup, at the smaller value of the voltage applied on the first GEM (350 V). One can see that at the minimum value of drift field providing a good transfer of electrons, around 250 Vcm^{-1}, the ion feedback fraction is only

2%. Decreasing the GEM voltage towards a condition of simple electron transmission (met around 200 V), the ion feedback can be reduced to less than 1%. This is a very important parameter to minimize in view of the possible use of GEMs as readout element of large volume drift chambers. Combining a suitable design of the GEM geometry, and several GEMs in cascade, it seems possible to reduce the ion feedback into the large drift volume of a TPC to a fraction small enough to avoid having recourse to active electrode gating. Further improvements on this point may be possible exploiting the peculiar asymmetric charge transmission properties of conical multipliers.

8. CONCLUSIONS AND SUMMARY

A systematic study of the distribution of electron and ion currents in standard GEM devices under uniform irradiation, in a wide range of voltages and fields, has unveiled several fundamental and interesting properties of the structures, here briefly summarized:

- The effective gain increases exponentially with the voltage applied across GEM, and almost linearly with the strength of the induction field; for a given voltage, it is larger for narrower holes, but independent of the pitch.
- At high values of induction field, dynamic changes of gain due to charging up are negligible, up to the highest gains and irradiation rates .
- The collection efficiency (or transparency) from the drift region into GEM, above few hundred Vcm^{-1}, is constant and close to unity, until reaching a drift field of several $kVcm^{-1}$; the limit is higher for higher GEM voltages, and for electrodes with larger optical transparency.
- Operation in strong magnetic fields is favored by the use of gas mixtures with small Lorentz angle (enriched with a molecular quencher), and by the choice of a geometry allowing the use of high drift fields (higher optical transparency).
- Charge collection and transfer features can be described by simple functions of the ratio of external and average internal GEM fields; the fields on the two sides of GEM have negligible mutual influence.
- The sharing of currents between electrodes is consistent with the assumption of an almost uniform spread of the avalanche in the holes, with electrons and ions invading all available field lines.
- The two multipliers in a double GEM structure operate essentially independently, with the first serving as injector into the second; the electron diffusion is large enough to obliterate the hole structure.
- The fractional ion feedback into the drift region is controlled by the applied fields and depends on the GEM geometry; in condition of full collection efficiency for electrons, it can be reduced to a few percent with a double structure.

In conclusion, the present study confirms that the gas electron multiplier performs with gains and charge distributions predictable from general electrostatic considerations and avalanche development models.

APPENDIX 1: ELECTRON DRIFT PROPERTIES IN SOME GAS MIXTURES

The charge transfer properties described in this study are largely independent of the nature of the gas, except for what concerns avalanche multiplication. Timing and localization properties of the detectors, however, depend on the electron drift and diffusion properties; for operation in magnetic fields, the relevant parameter is the Lorentz deflection angle. We reproduce in Figs. A1 to A3 the computed field dependence of electron drift velocity, diffusion and Lorentz angle for perpendicular electric and magnetic fields, for two gas mixtures mentioned it the text: argon-CO_2 in the volume proportions 70-30, and argon-DME 30-70[5]. Using a standard GEM design, full collection efficiency from the drift region is obtained at fields up to 3-4 $kVcm^{-1}$ (cf. Fig. 21). In the Ar-CO_2 mixture, the fast electron drift velocity at these values of field is suitable for high rate applications; in presence of moderate external magnetic fields, the Lorentz deflection angle has also acceptable values. For operation at higher magnetic fields, on the other hand, the DME-rich mixture is preferable, but requires the use of rather high values of drift field in order to reach a sufficiently fast drift velocity; this implies the necessity of using a GEM design with larger optical transparency.

APPENDIX 2: GRID TRANSPARENCY

The charge transmission efficiency τ from a region of field E_1 into a field E_2, separated by the mesh, is given by the following expression [20]:

$$\tau = 1 - \frac{1}{\pi}\left\{\rho(R+1)\sqrt{1-\left(\frac{1}{\rho}\frac{R-1}{R+1}\right)^2} - (R-1)\cos^{-1}\left(\frac{1}{\rho}\frac{R-1}{R+1}\right)\right\}$$

where $R = E_2 / E_1$, and $\rho = 2\pi r / d$ is a parameter expressing the opacity of a grid of parallel wires of radius *r* at a distance *d*. Gradually increasing as a function of *R*, the electrical transparency tends to unity with a slope that depends on the geometrical opacity. The permitted range of R in the expression is determined by the opacity:

$$\frac{1-\rho}{1+\rho} < R < \frac{1+\rho}{1-\rho}.$$

Owing to the one-dimensional nature of the solution, we have attempted to fit the values of electron transparency measured with the two-dimensional GEM mesh with the square of the previous expression (see section 7).

APPENDIX 3: POWER SUPPLY SCHEMES

Various schemes have been used to apply the operating voltages to the multi-electrode structures described; all have drawbacks, and in some cases lead to diverging operation in presence of heavy radiation fluxes:

- Individual power supplies (Fig.A4a). Each electrode is independently connected, through a large value protection resistor R (several MΩ), to a low noise, current limited high voltage unit. The scheme is convenient for systematic studies, since it permits to vary the potential difference between

[5] Computed with S. Biagi's program MAGBOLTZ.

any pair of electrodes, keeping constant all others; it requires however a patient procedure for rising the voltages, in order to avoid exceeding maximum local differences. Under heavy irradiation, the potential drop on the serial protection resistor can be estimated and corrected. For the single GEM, with positive and, respectively, negative currents on the top and bottom electrodes, the result of irradiation is always a drop of the multiplying voltage difference, and therefore a safe operation. We have found however that the reverse electron current can generate problems, depending on the power supply unit characteristics; also, in case of discharges, the current from one unit can feed into the other with unpredictable results. A solution to the problems is to drag from each unit a leakage current with a suitable large value resistor R_L connected to ground (dashed in the figure).

In the double GEM detector, a dangerous situation can be encountered in the first multiplier if the (positive) current on the bottom electrode exceeds the one on the top; such is the case for example in the conditions of Fig. 26 above a critical value of transfer field. In this case, under heavy irradiation, the difference of potential across the first multiplier increases, potentially leading to a diverging operation. It should be noted that this is the case of all double devices, where a GEM is followed by another multiplier, generating positive ions.

- For long term studies and beam exposures we have used simpler resistive partition networks to provide the potentials, either from a single supply to all electrodes, or separately for each GEM, Fig. A4b and c. The upper drift electrode is usually powered independently. This scheme permits an easier ramp up of the voltages, but constrains the ratios of potentials to pre-determined values. To obtain a reasonable stability of operation, the polarization current in the resistor chain should be much larger than the maximum difference in signal currents; in the event of a discharge, all potentials drop, reducing the risk of local over-voltage.

As for the previous case, the potential difference across GEM can increase under heavy exposure leading to a dangerous positive feedback situation. When using separate resistor chains for the two multipliers, and with reference to the schematics in Fig. A4b, a diverging situation is found when $I_B > I_T R_3 / R_1$., a circumstance that can be met on the first GEM in a cascaded detector. Equivalent expressions can be written for the scheme of Fig. A4c.

A powering system making use of individual floating supplies, cascaded in a chain and with efficient over-voltage and current protection, should solve of the above mentioned problems[6]. It is certain that the development of more appropriate high voltage distribution systems is indispensable to insure better reliability and safer operation of GEM-based detectors in experimental setups subjected to heavy irradiation.

[6] A modular HV system satisfying these requirements is produced by CAEN, Viareggio, Italy.

REFERENCES

[1] F. Sauli, Nucl. Instrum. and Meth. **A386** (1997) 531.
[2] R. Bouclier, M. Capeáns, W. Dominik, M. Hoch, J.-C. Labbé, G. Million, L. Ropelewski, F. Sauli, A. Sharma, IEEE Trans. Nucl. Sci. **NS-44** (1997) 646.
[3] R. Bouclier, W. Dominik, M. Hoch, J.C. Labbé, G. Million, L. Ropelewski, F. Sauli, A. Sharma, G. Manzin, Nucl. Instrum. and Meth. **A396** (1997) 50.
[4] J. Benlloch, A. Bressan, M. Capeáns, M. Gruwé, M. Hoch, J.C. Labbé, A. Placci, L. Ropelewski, F. Sauli, Nucl. Instrum. and Meth. **A 419** (1998) 410.
[5] J. Benlloch, A. Bressan, C. Büttner, M. Capeáns, M. Gruwé, M. Hoch, J.C. Labbé, A. Placci, L. Ropelewski, F. Sauli, A. Sharma, R. Veenhof, IEEE Trans. Nucl. Sci. **NS-45** (1998) 234.
[6] C. Büttner, M. Capeáns, W. Dominik, M. Hoch, J.C. Labbé, G. Manzin, G. Million, L. Ropelewski, F. Sauli, A. Sharma, Nucl. Instrum. and Meth. **A 409** (1998) 79.
[7] W. Beaumont, T. Beckers, J. DeTroy, V. Van Dyck, O. Bouhali, F. Udo, C. VanderVelde, W. Van Doninck, P. Vanlaer, V. Zhukov, Nucl. Instrum. and Meth. **A 419** (1998) 394.
[8] R. Bellazzini, A. Brez, G. Gariano, L. Latronico, N. Lumb, G. Spandre, M.M. Massai, R. Raffo, M.A. Spezziga, Nucl. Instrum. and Meth. **A 419** (1998) 429.
[9] A. Bressan, J.C. Labbé, P. Pagano, L. Ropelewski, F. Sauli, Nucl. Instrum. and Meth. **A425** (1999) 262.
[10] A. Bressan, L. Ropelewski, F. Sauli, D. Mörmann, T. Müller, H.J. Simonis, Nucl. Instrum. and Meth. **A425** (1999) 254.
[11] R. Chechik, A. Breskin, G. Garty, J. Mattout, F. Sauli, E. Shefer, Nucl. Instrum. and Meth. **A419** (1998) 423.
[12] A. Bondar, A. Buzulutskov, F. Sauli, L. Shekhtman, Nucl. Instrum. and Meth. **A 419** (1998) 418.
[13] G. Garty, R. Chechik, A. Breskin, E. Shefer, Single photoelectron detection with a low pressure GEM coupled to a CsI photocathode, Int. Workshop on Ring Imaging Cherenkov Detectors RICH98 (Ein-Gedi, Dead Sea, Israel, November 15-20, 1998). Subm. Nucl. Instrum. and Meth. (1998).
[14] B. Schmidt, Nucl. Instrum. and Meth. **A 419** (1998) 230.
[15] L.L. Jones, PreMux Specifications, v. 2.3, Internal Note (1995).
[16] R. Veenhof, Nucl. Instum. and Meth. **A419** (1998) 726.
[17] T. Beckers, R. Bouclier, C. Garabatos, G. Million, F. Sauli, L. Shekhtman, Nucl. Instrum. and Meth. **A346** (1994) 95.
[18] A. Bressan, M. Hoch, P. Pagano, L. Ropelewski, F. Sauli, S. Biagi, A. Buzulutskov, M. Gruwé, A. Sharma, D. Moermann, G. De Lentdecker, Nucl. Instrum. and Meth. **A424** (1998) 321.
[19] W. Beaumont, T. Beckers, O. Bouhali, J. De Troy, F. Udo, C. Vander Velde, W. Van Doninck, C. Van Dyck, L. Vanlaer, V. Zhukov, Proc. Sixth Int. Conf. on Advanced Technology and Particle Physics (Como, Italy, 7-11 October 1998) .
[20] O. Bunemann, T.E. Cranshaw, J.A. Harvey, Canadian J. of Res. **27A** (1949) 191.

FIGURE CAPTIONS

Fig. 1: Schematics of the standard (a and b) and conical GEM geometry.
Fig. 2: Two examples of electrodes with large (a) and small transparency (b).
Fig. 3: Schematics of the single (a) and double (b) GEM detectors.
Fig. 4: Collection efficiency as a function of drift field on the method of measurement: integral current or pulse with two time constants.
Fig. 5: Drift collection efficiency for soft X-rays and fast electrons.
Fig. 6: Electric field map in a typical operating condition.
Fig. 7: Field map in conditions of reduced collection efficiency.
Fig. 8: Optimized conditions for operation in moderate magnetic fields.
Fig. 9: Optimized conditions for operation in high magnetic fields.
Fig. 10: Electric field computed along a line through the center of the holes, for different hole diameters.
Fig. 11: Electric field computed along lines parallel to the electrode at different distances from the center.
Fig. 12: Effective gain as a function of voltage in typical operating conditions.
Fig. 13: Effective and real gain as a function of hole diameters.
Fig. 14: Current sharing between electrodes in the single GEM detector, as a function of the induction field, for a low (a) and high (b) drift field value.
Fig. 15: Signal shape in the electron collection mode and at the onset of the parallel plate multiplication. Horizontal scale: 500 ns / division.
Fig. 16: Effective gain as a function of induction field in a range of gas mixtures and GEM voltages, adjusted to obtain similar gains.
Fig. 17: Maximum GEM operating voltage under heavy irradiation as a function of induction field, and corresponding effective gains.
Fig. 18: Time dependence of gain, showing a small increase due to charging up only for low values of the induction field.
Fig. 19: Current sharing between electrodes as a function of drift field, for a small (a) and large (b) GEM voltage, at a low induction field value (2 $kVcm^{-1}$). The X-ray irradiation rate was kept constant at around 10^4 $mm^{-2}s^{-1}$.
Fig. 20: Current sharing between electrodes as a function of drift field, for a small (a) and large (b) GEM voltage, at a high induction field value (8 $kVcm^{-1}$).
Fig. 21: Electron collection efficiency (transparency) as a function of drift field, for several values of GEM voltage and a low (a) and high (b) induction field.
Fig. 22: Transparency as a function of drift field measured on three GEMs with different geometry for low (a, 400 V) and high GEM voltage (b, 500 V).
Fig. 23: Ion feedback ratio as a function of drift field for several GEM voltages, at a low (a) and high induction field (b).
Fig. 24: Effective gain as a function of voltage of single and double GEM detectors, operated at similar values of the external fields.
Fig. 25: Effective gain in the double GEM detector in a range of values of operating voltages having constant sum.
Fig. 26: Electrode currents in the double GEM as a function of drift field for three choices of GEM voltages, having constant sum: 350 / 500 (a), 425 / 425 (b) and 500 / 350 (c).
Fig. 27: Electrode currents in the double GEM as a function of transfer field for three choices of GEM voltages, having constant sum: 350 / 500 (a), 425 / 425 (b) and 500 / 350 (c).
Fig. 28: Electrode currents in the double GEM as a function of induction field for three choices of GEM voltages, having constant sum: 350 / 500 (a), 425 / 425 (b) and 500 / 350 (c).

Fig. 29: Summary of measurements of the signal current in a range of GEM voltages as a function of drift (a), transfer (b) and induction field (c).
Fig. 30: Currents measured on the conical GEM as a function of drift field for an electron collection wide to narrow (a) and narrow to wide holes (b).
Fig. 31: Gain as a function of irradiation time in the conical GEM for a wide to narrow (a) and narrow to wide electron collection (b).
Fig. 32: Electron transparency as a function of the ratio between drift field and the field in the center of the holes, for several GEM with different geometry and operating voltage. Dashed lines are computed from a model.
Fig. 33: Fractional electron current as a function of drift field for several voltage sharing in the two GEMs.
Fig. 34: Fractional electron current as a function of drift field for two values of induction field.
Fig. 35: Fractional electron current as a function of the ratio between induction field and the field in the center of the holes.
Fig. 36: Fractional electron current as a function of transfer field.
Fig. 37: Fractional ion current on the drift electrode in the double GEM as a function of drift field.
Fig. 38: Expanded view for low drift fields of the measured ion feedback fraction and of the electron transparency in the double GEM detector.
Fig. A1: Drift velocity and diffusion (for one cm drift) in argon-carbon dioxide at STP in the volume proportions 70-30.
Fig. A2: Drift velocity and diffusion (for one cm drift) in argon-dimethylether at STP in the volume proportions 30-70.
Fig. A3: Lorentz angle as a function of field for the Ar-CO_2 70-30 and Ar-DME 30-70 mixtures.
Fig. A4: Power supply schemes used to apply voltages to the GEM detectors: individual connection (a), single (b) and double resistor network (c).

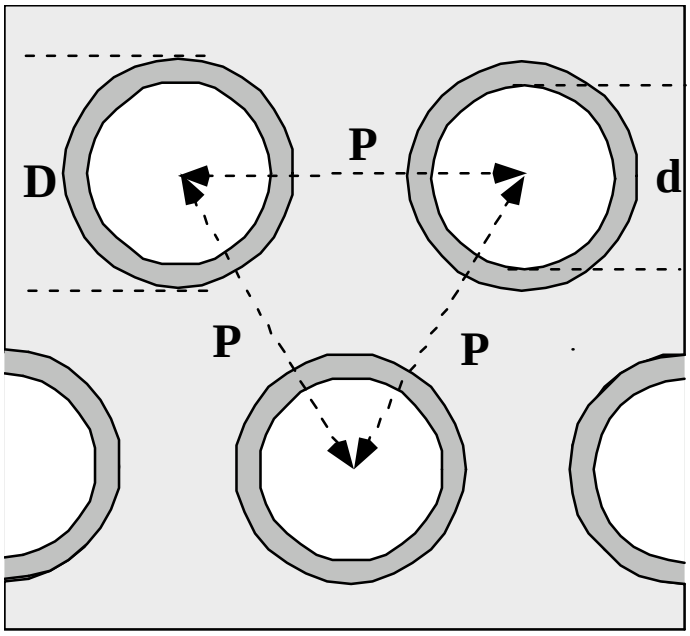

(a)

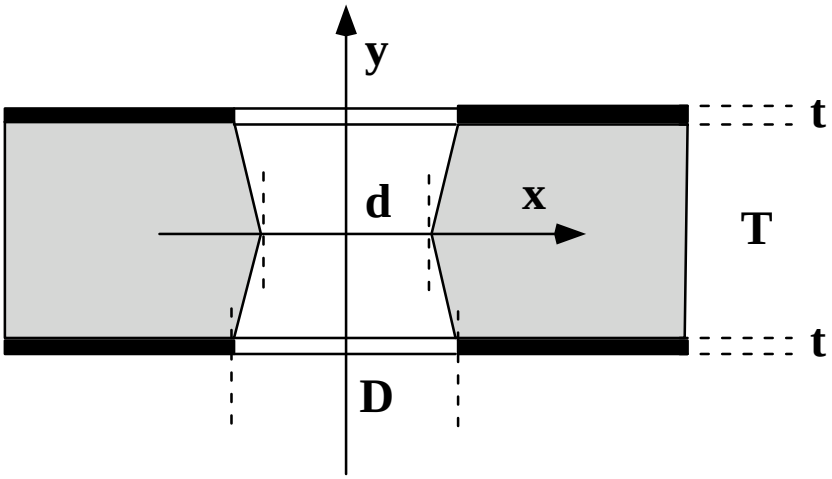

(b)

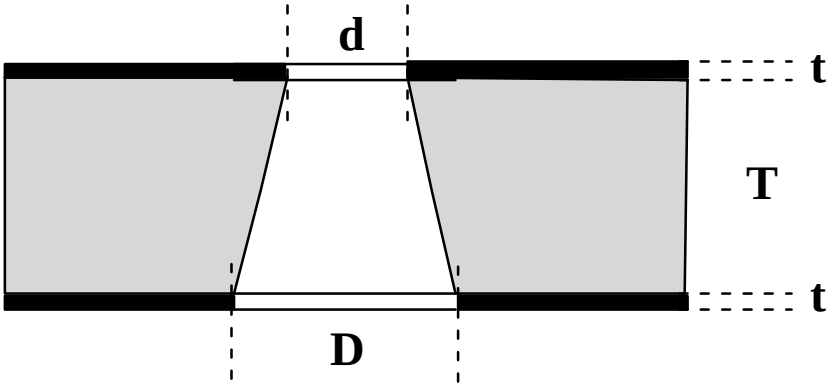

(c)

Fig. 1

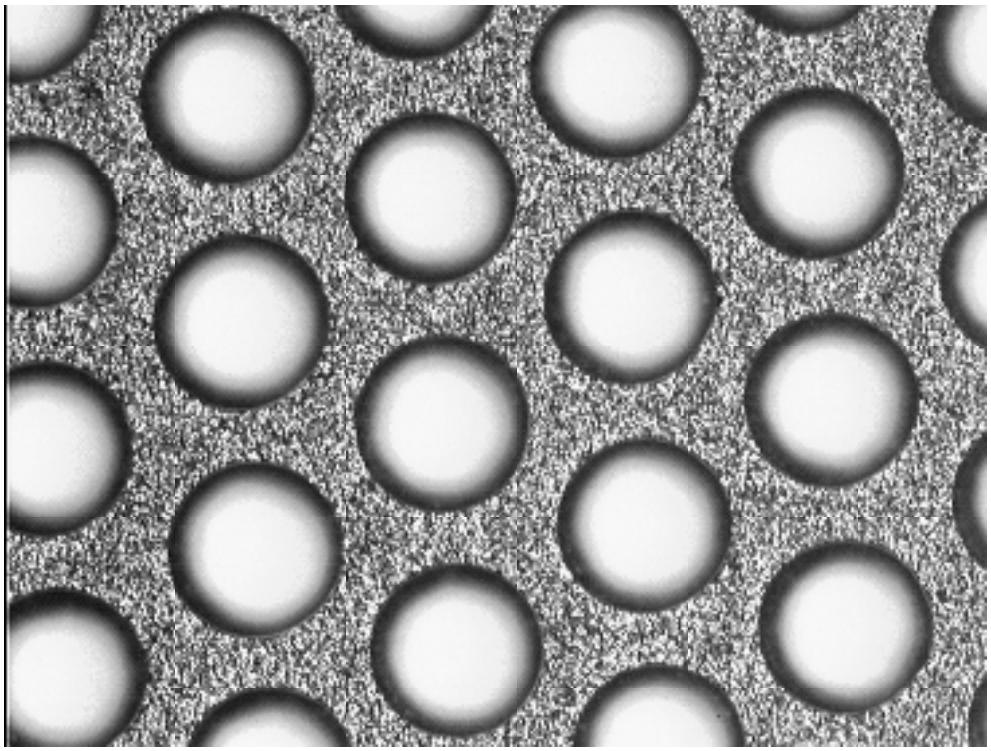

(a)

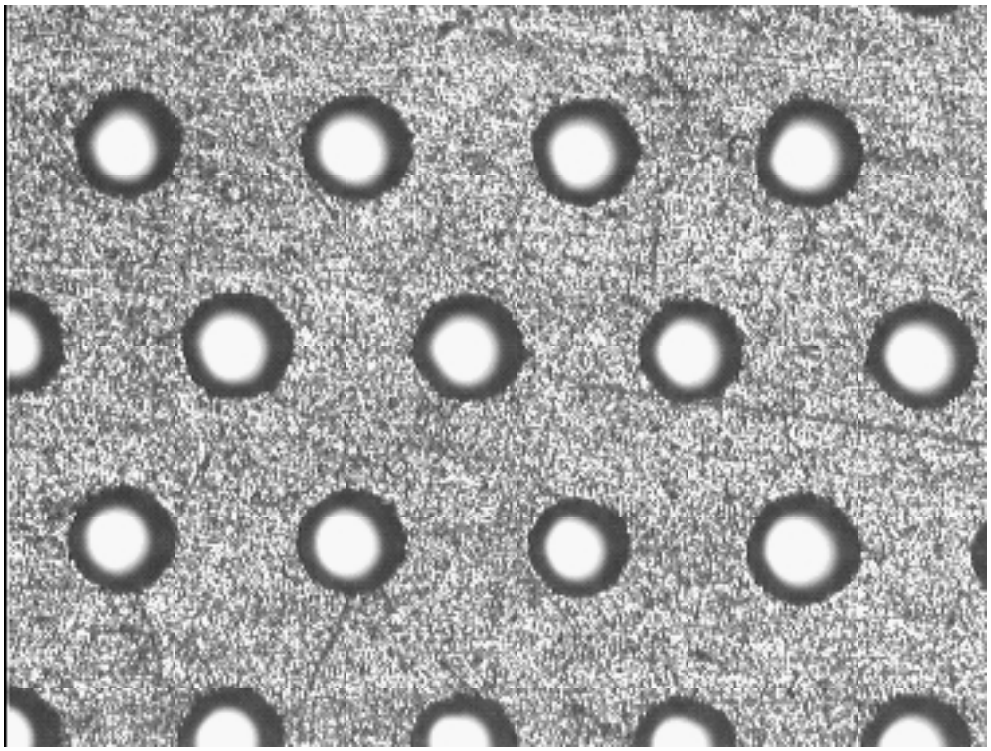

(b)

Fig. 2

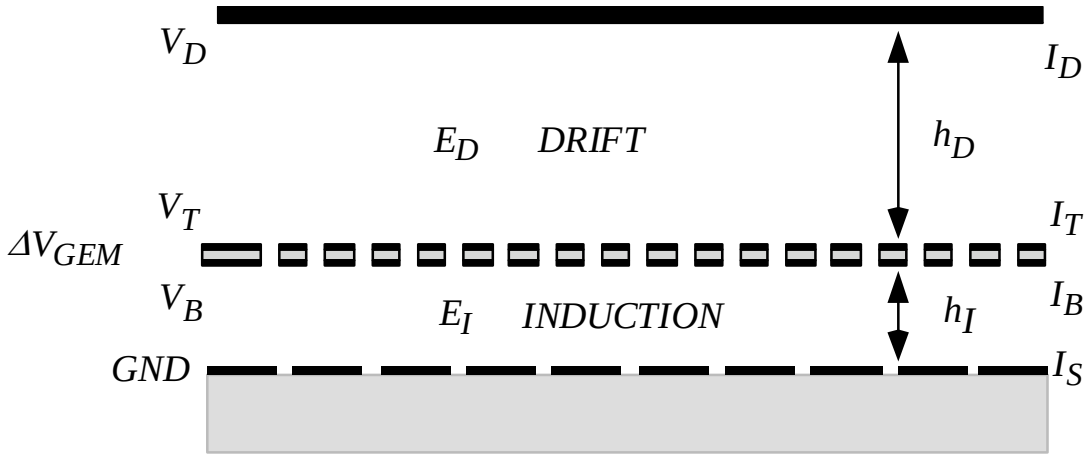
V_D
I_D
E_D DRIFT
h_D
V_T
I_T
ΔV_{GEM}
V_B
E_I INDUCTION
h_I
I_B
GND
I_S

(a)

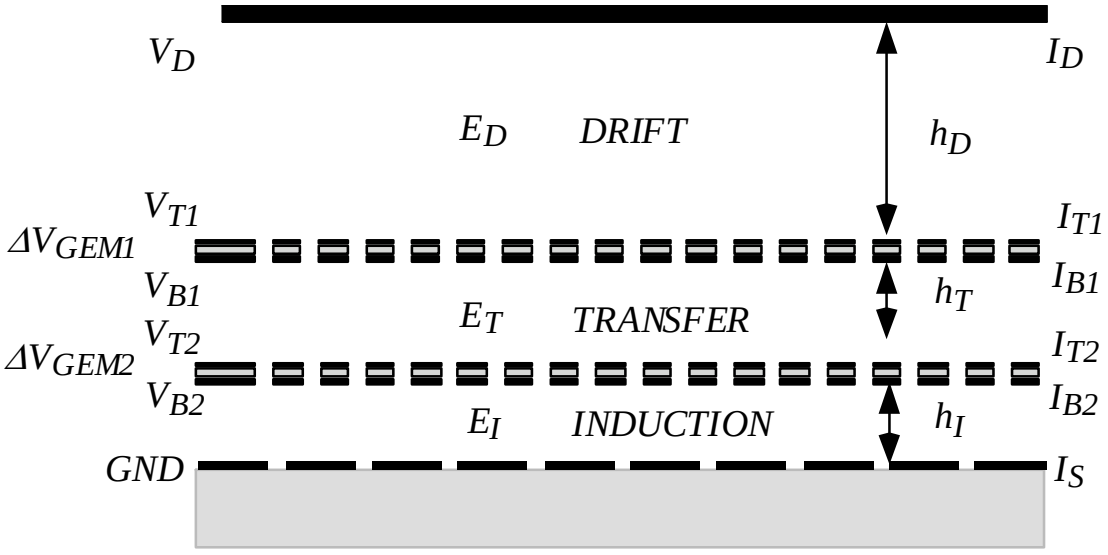
V_D
I_D
E_D DRIFT
h_D
V_{T1}
I_{T1}
ΔV_{GEM1}
V_{B1}
I_{B1}
h_T
E_T TRANSFER
V_{T2}
I_{T2}
ΔV_{GEM2}
V_{B2}
I_{B2}
E_I INDUCTION
h_I
GND
I_S

(b)

Fig. 3

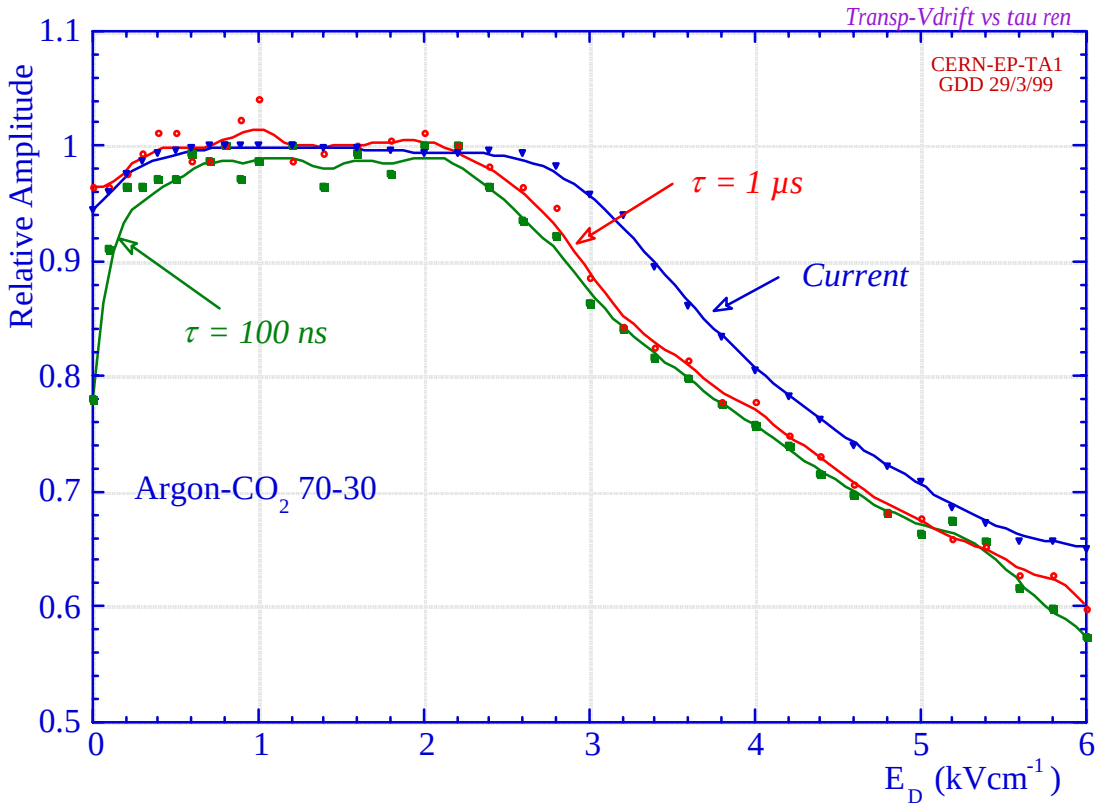
Transp-Vdrift vs tau ren
CERN-EP-TA1
GDD 29/3/99
Relative Amplitude
τ = 1 μs
Current
τ = 100 ns
Argon-CO2 70-30
E_D (kVcm^-1)

Fig. 4

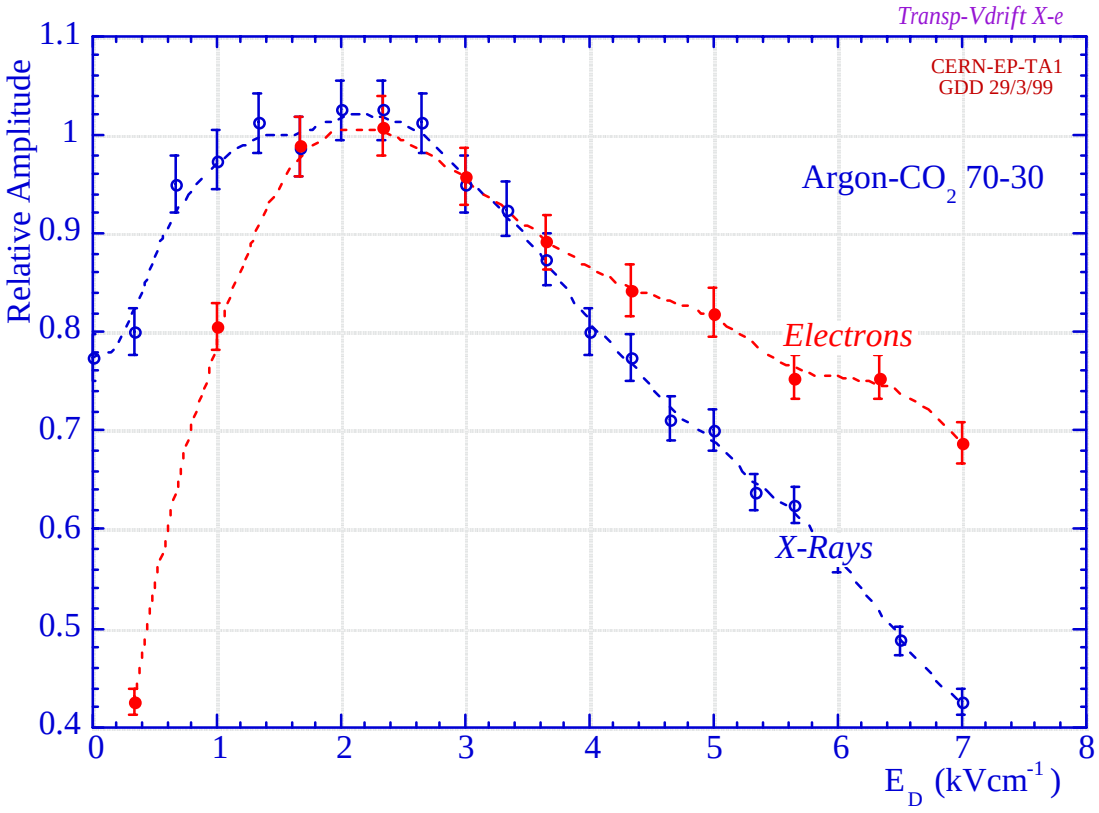
Transp-Vdrift X-e
CERN-EP-TA1
GDD 29/3/99
Relative Amplitude
Argon-CO2 70-30
Electrons
X-Rays
E_D (kVcm^-1)

Fig. 5

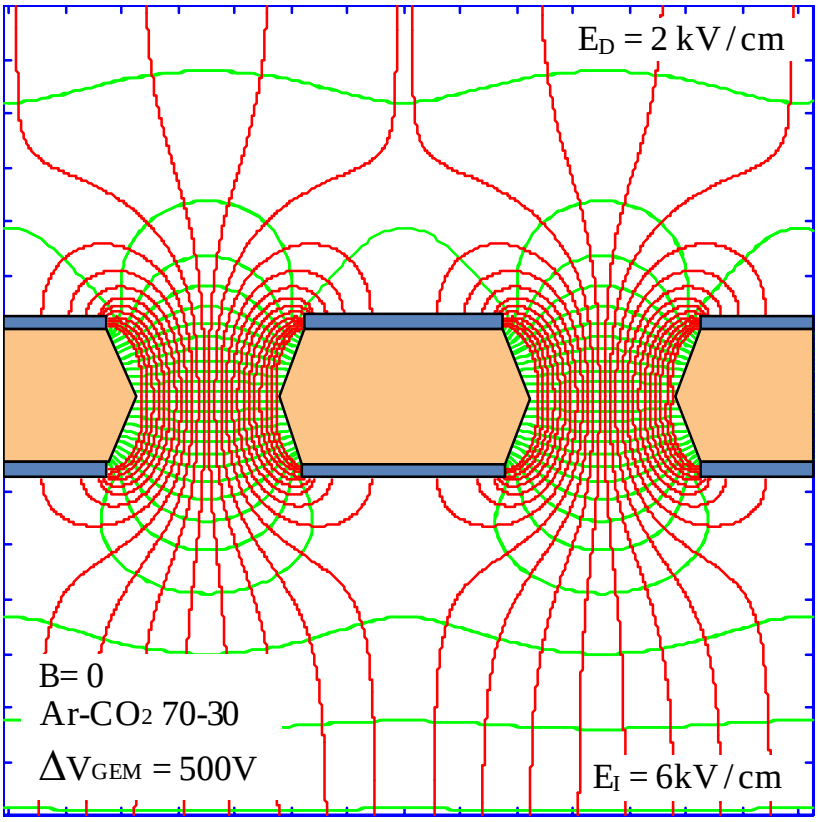
E_D = 2 kV / cm
B= 0
Ar-CO2 70-30
ΔVGEM = 500V
E_I = 6kV / cm

Fig. 6

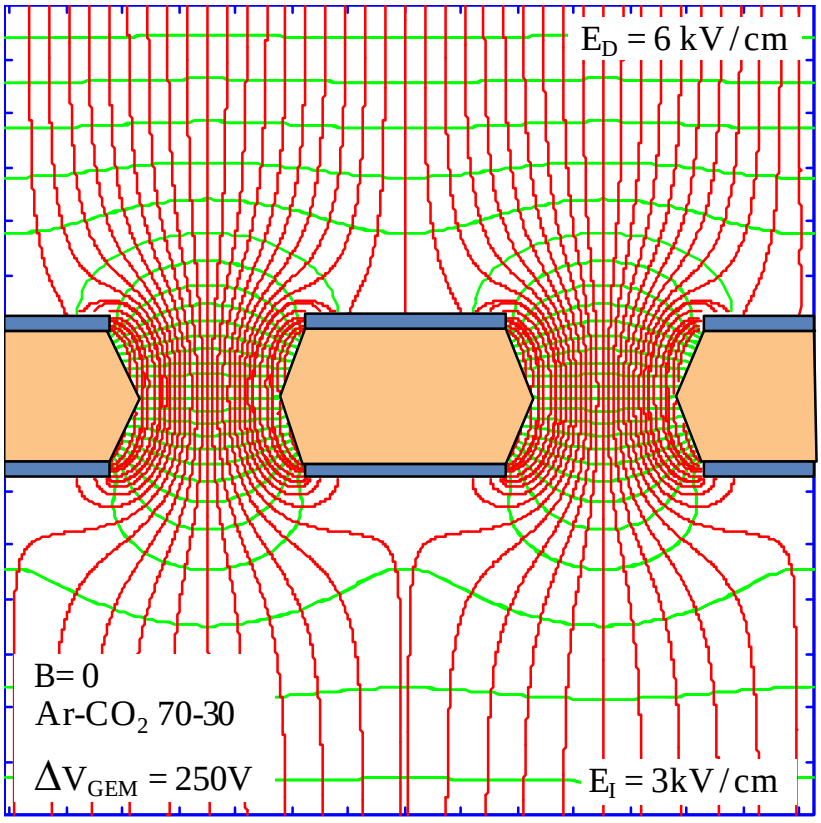
E_D = 6 kV / cm
B= 0
Ar-CO2 70-30
ΔV_GEM = 250V
E_I = 3kV / cm

Fig. 7

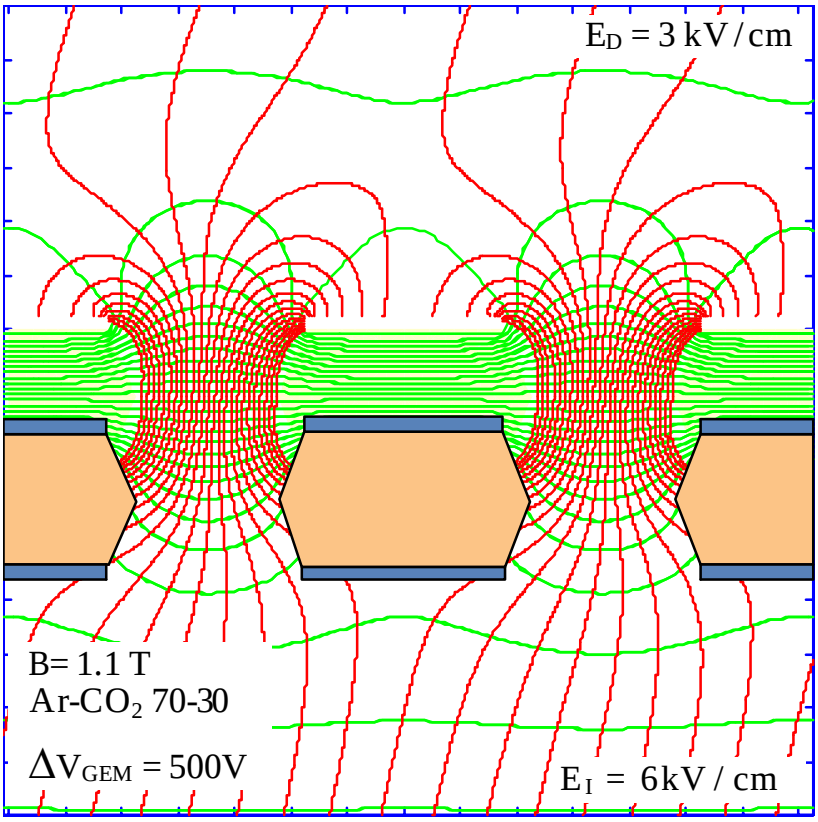
E_D = 3 kV / cm
B= 1.1 T
Ar-CO_2 70-30
ΔV_{GEM} = 500V
E_I = 6kV / cm

Fig. 8

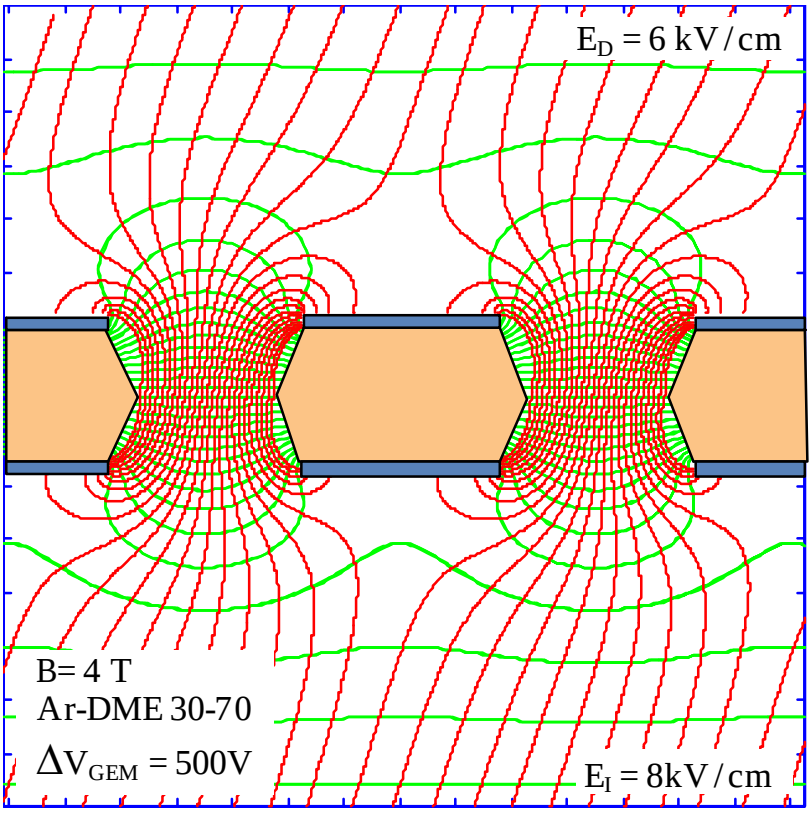
E_D = 6 kV / cm
B= 4 T
Ar-DME 30-70
ΔV_{GEM} = 500V
E_I = 8kV / cm

Fig. 9

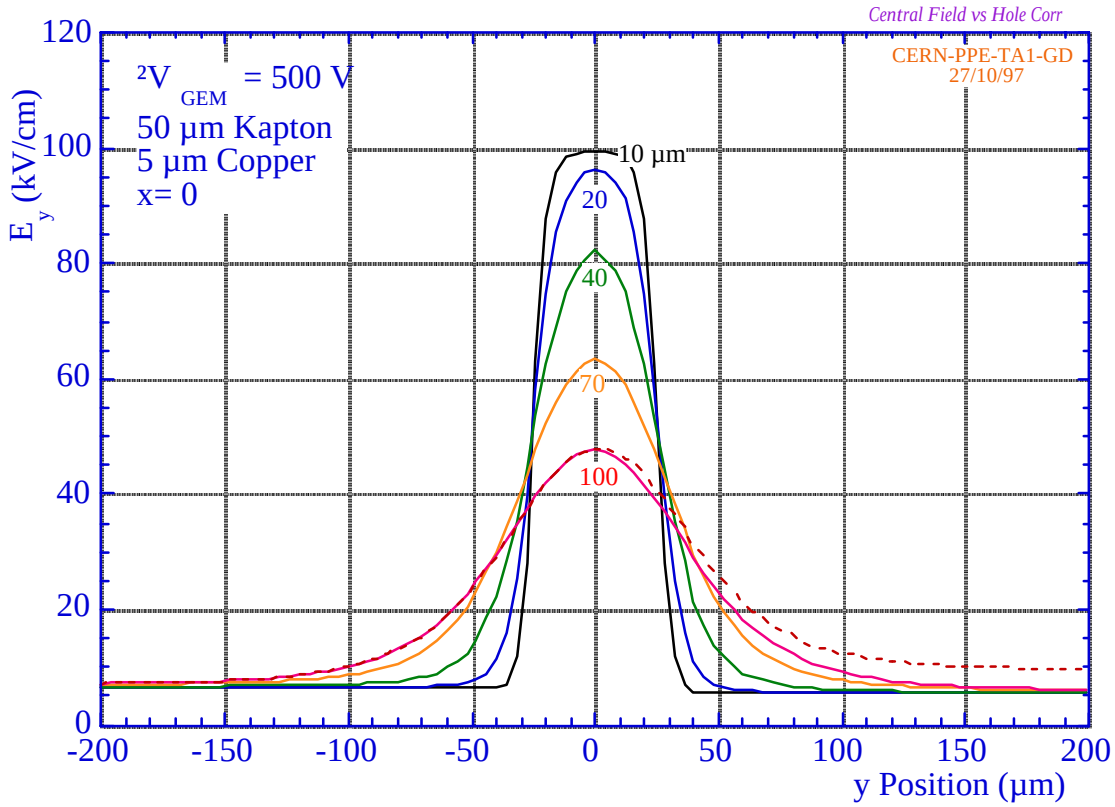
Central Field vs Hole Corr
CERN-PPE-TA1-GD
27/10/97
²V GEM = 500 V
50 µm Kapton
5 µm Copper
x= 0
10 µm
20
40
70
100
E_y (kV/cm)
y Position (µm)

Fig. 10

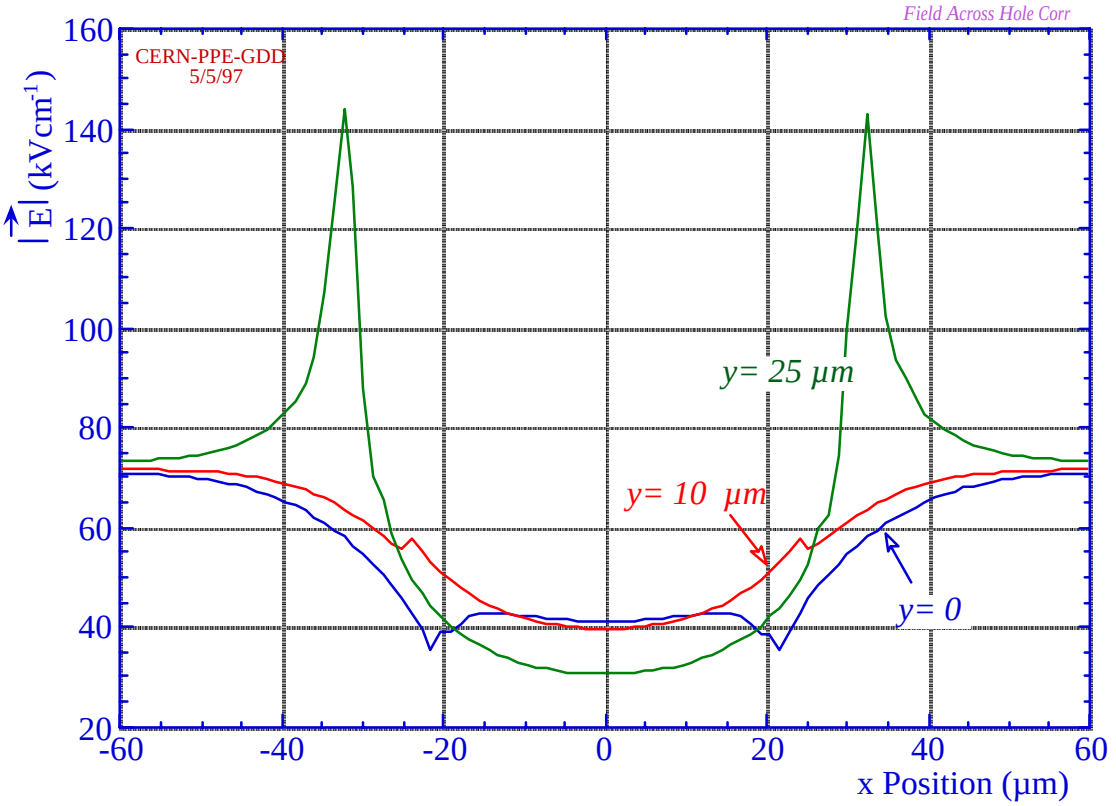
Field Across Hole Corr
CERN-PPE-GDD
5/5/97
|E| (kVcm⁻¹)
y= 25 µm
y= 10 µm
y= 0
x Position (µm)

Fig. 11

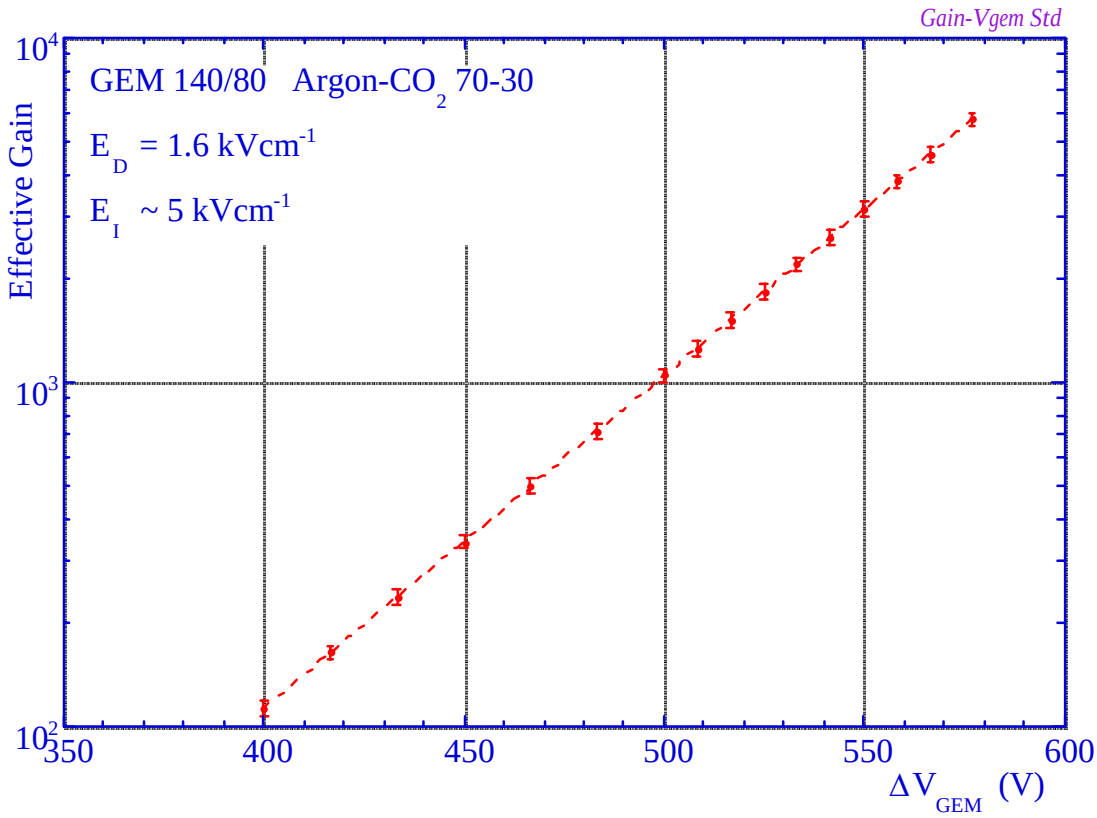
Gain-Vgem Std
GEM 140/80 Argon-CO2 70-30
ED = 1.6 kVcm-1
EI ~ 5 kVcm-1
Effective Gain
ΔVGEM (V)

Fig. 12

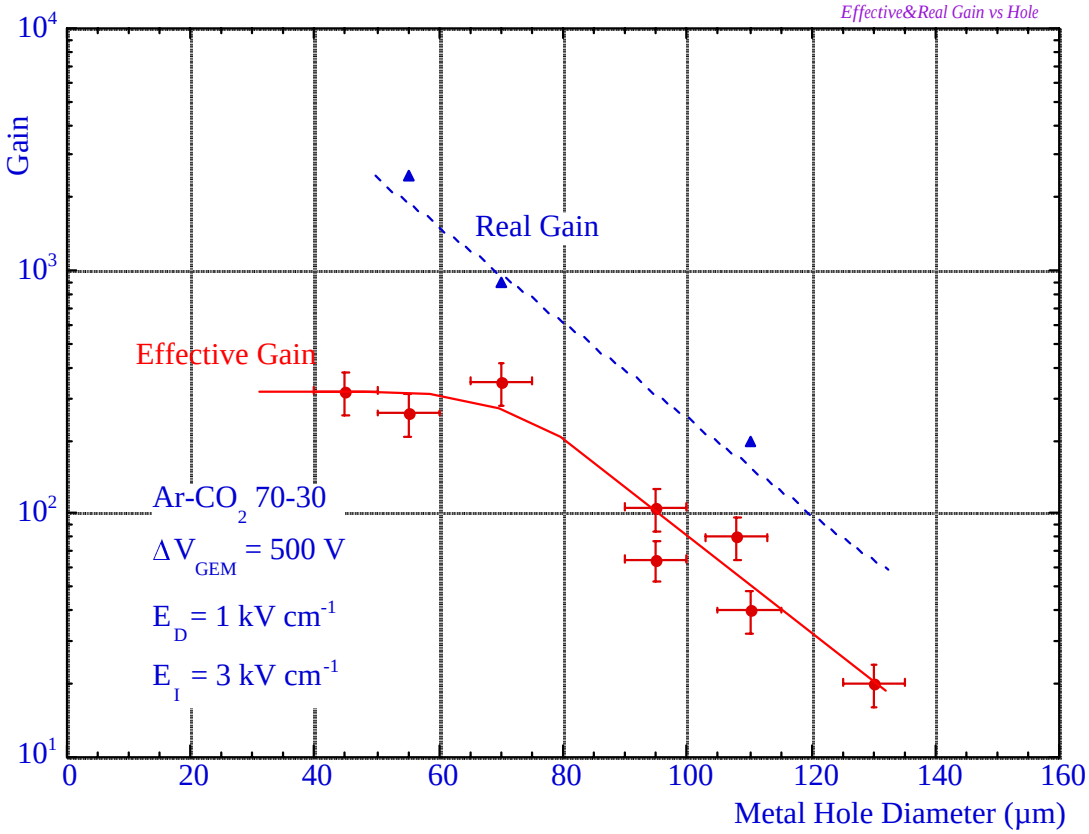
Effective&Real Gain vs Hole
Gain
Real Gain
Effective Gain
Ar-CO2 70-30
ΔVGEM = 500 V
ED = 1 kV cm-1
EI = 3 kV cm-1
Metal Hole Diameter (μm)

Fig. 13

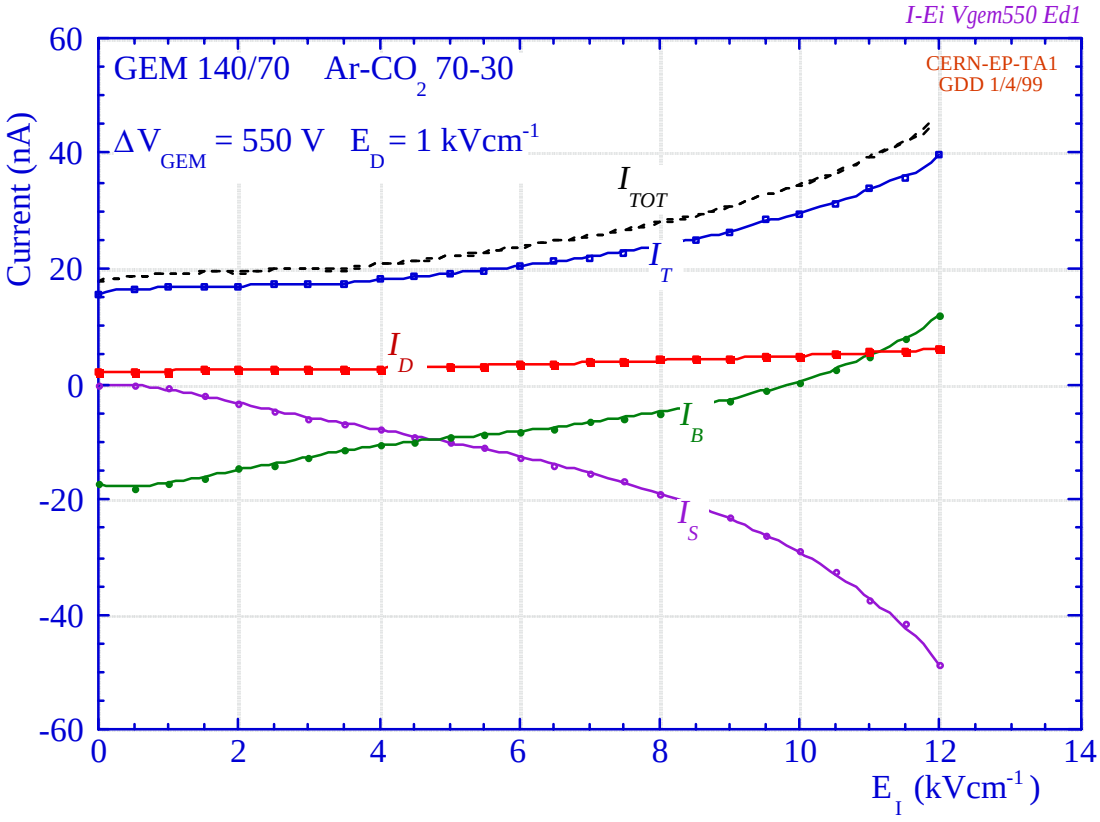

Fig. 14 (a)

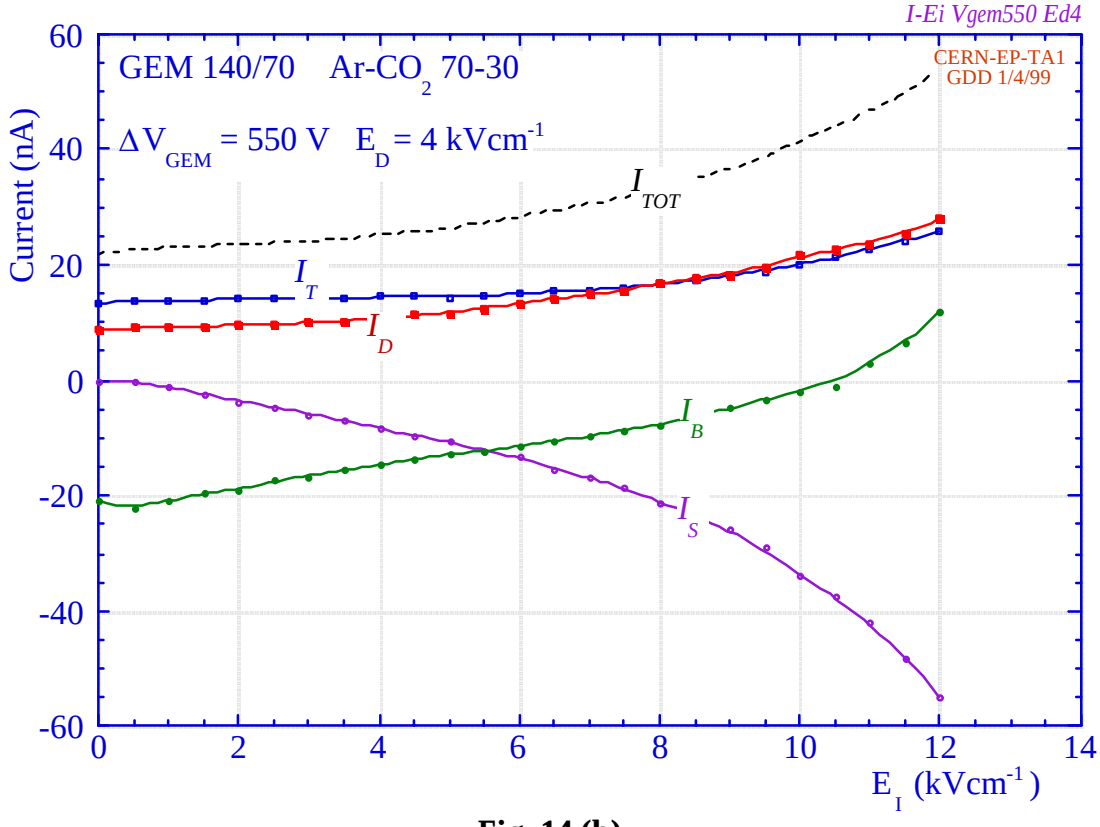

Fig. 14 (b)

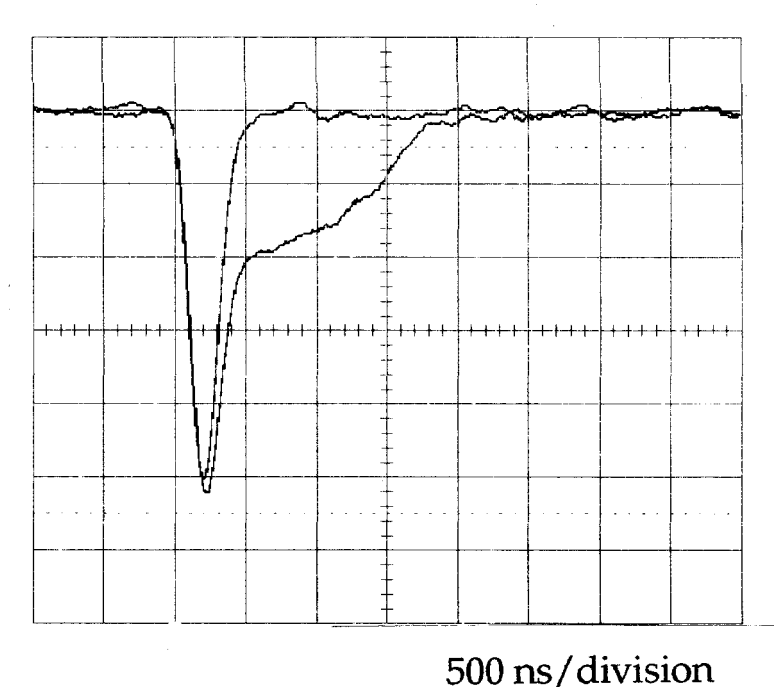
500 ns/division

Fig. 15

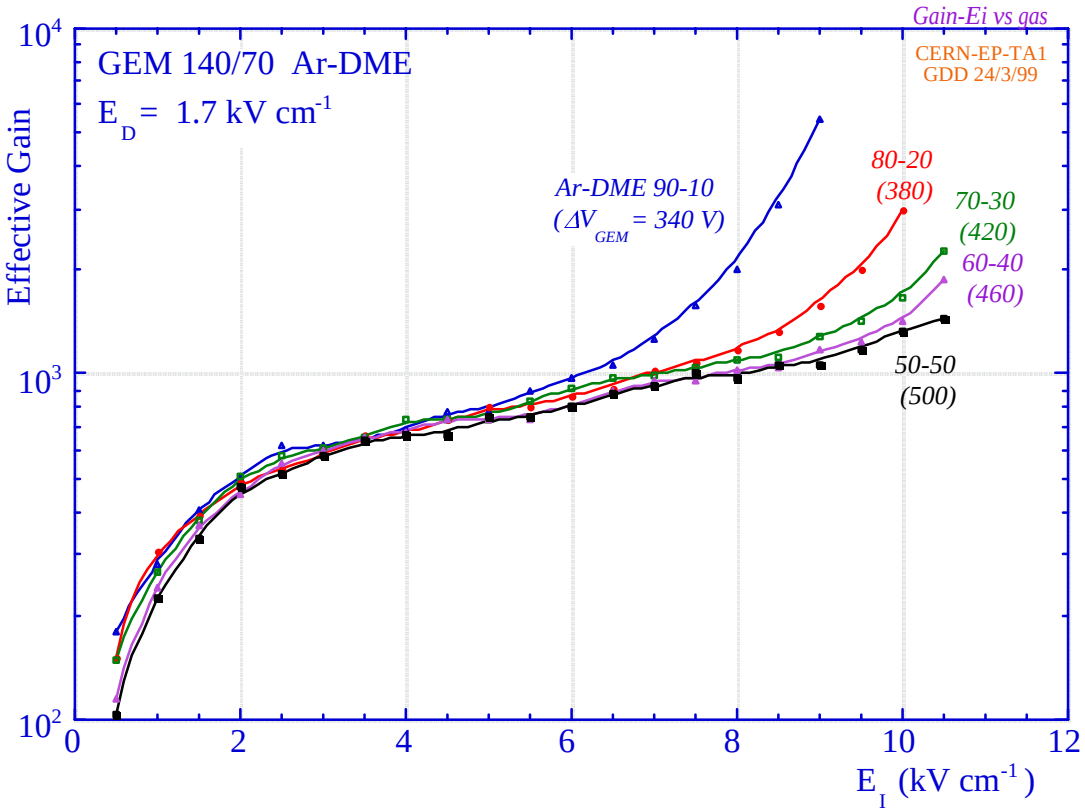
Gain-Ei vs gas
CERN-EP-TA1
GDD 24/3/99
GEM 140/70 Ar-DME
E_D = 1.7 kV cm^-1
Ar-DME 90-10
(ΔV_GEM = 340 V)
80-20
(380)
70-30
(420)
60-40
(460)
50-50
(500)
Effective Gain
10^4
10^3
10^2
0
2
4
6
8
10
12
E_I (kV cm^-1)

Fig. 16

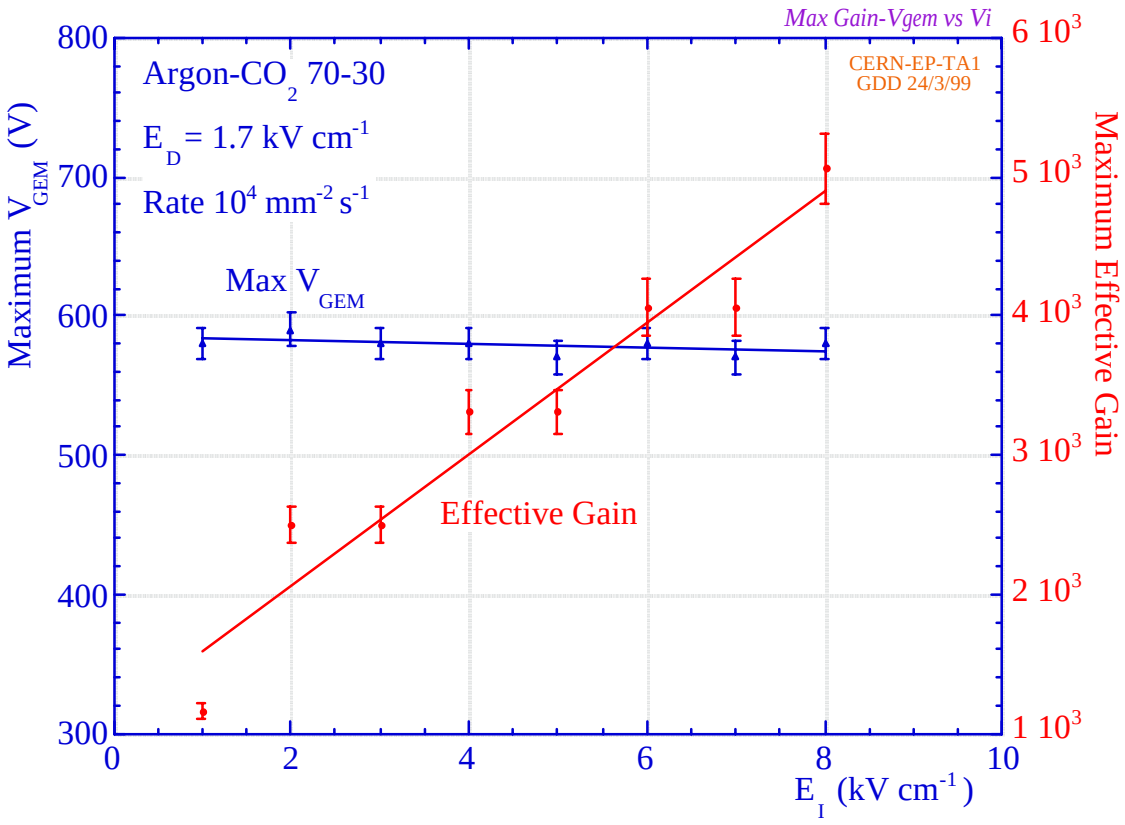
Max Gain-Vgem vs Vi
CERN-EP-TA1
GDD 24/3/99
Argon-CO2 70-30
ED = 1.7 kV cm-1
Rate 10^4 mm-2 s-1
Max VGEM
Effective Gain
Maximum VGEM (V)
Maximum Effective Gain
EI (kV cm-1)
800
700
600
500
400
300
6 10^3
5 10^3
4 10^3
3 10^3
2 10^3
1 10^3
0
2
4
6
8
10

Fig. 17

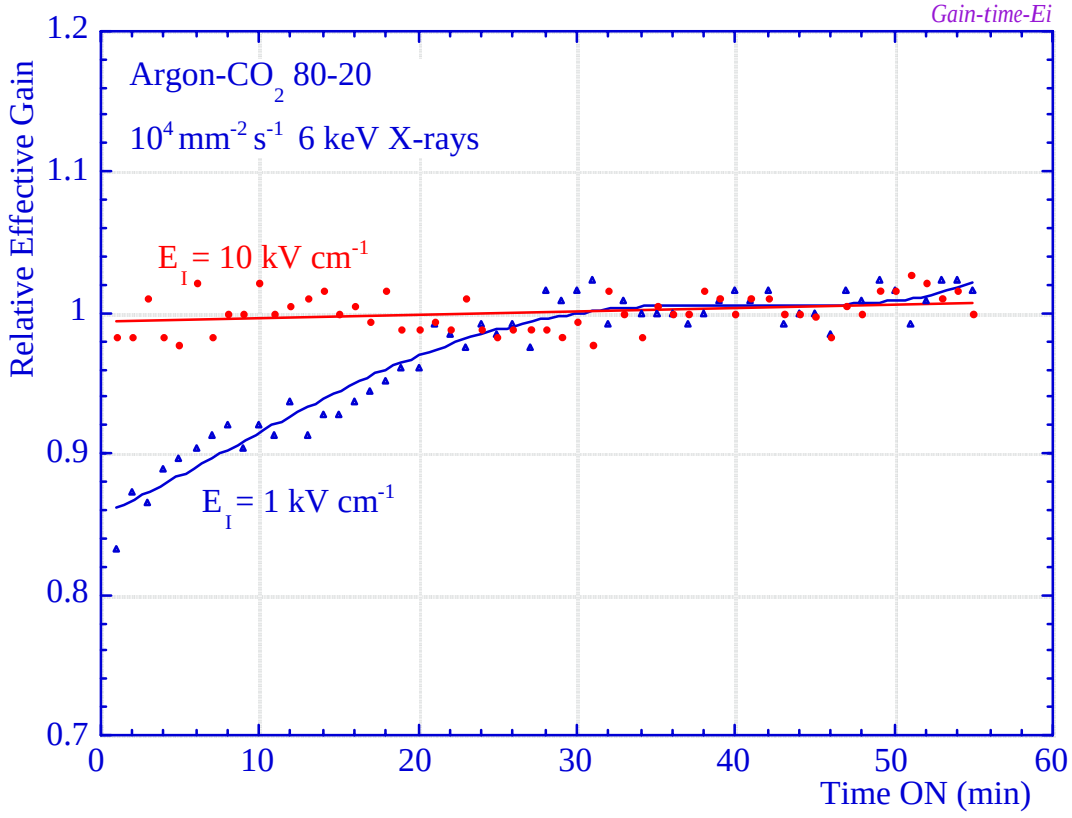
Gain-time-Ei
Argon-CO2 80-20
10^4 mm-2 s-1 6 keV X-rays
EI = 10 kV cm-1
EI = 1 kV cm-1
Relative Effective Gain
Time ON (min)
1.2
1.1
1
0.9
0.8
0.7
0
10
20
30
40
50
60

Fig. 18

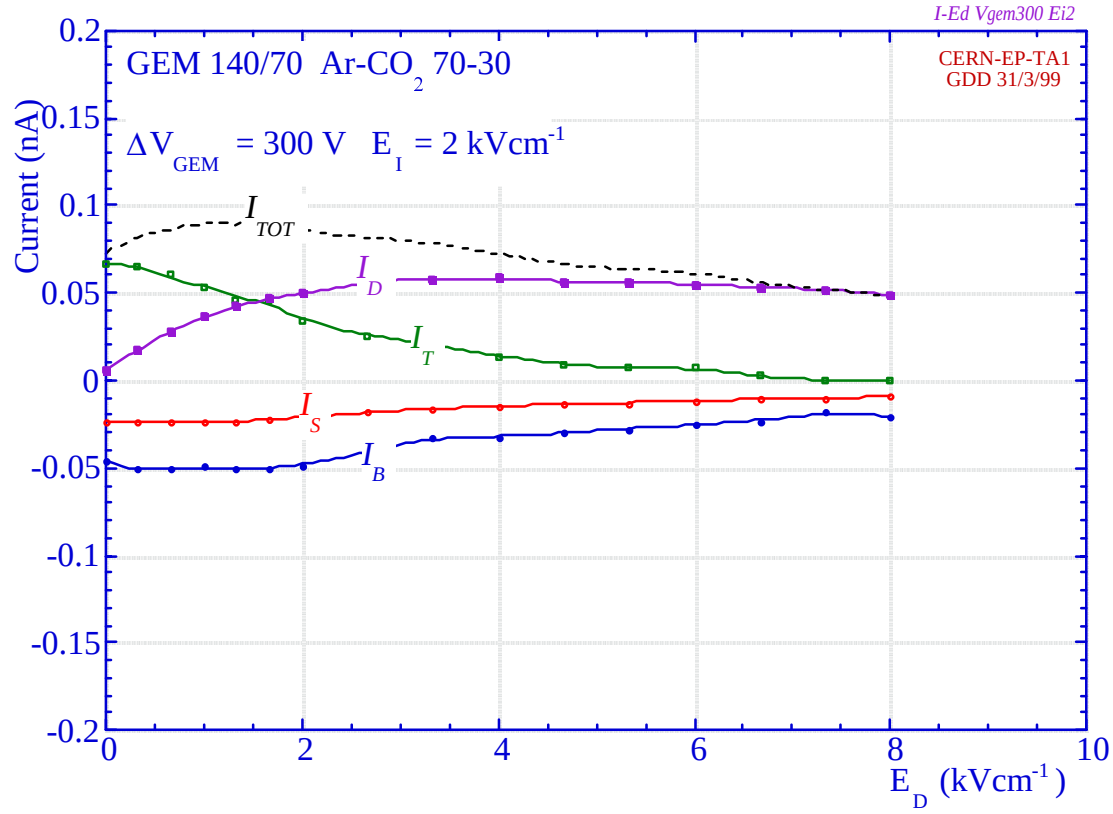

Fig. 19 (a)

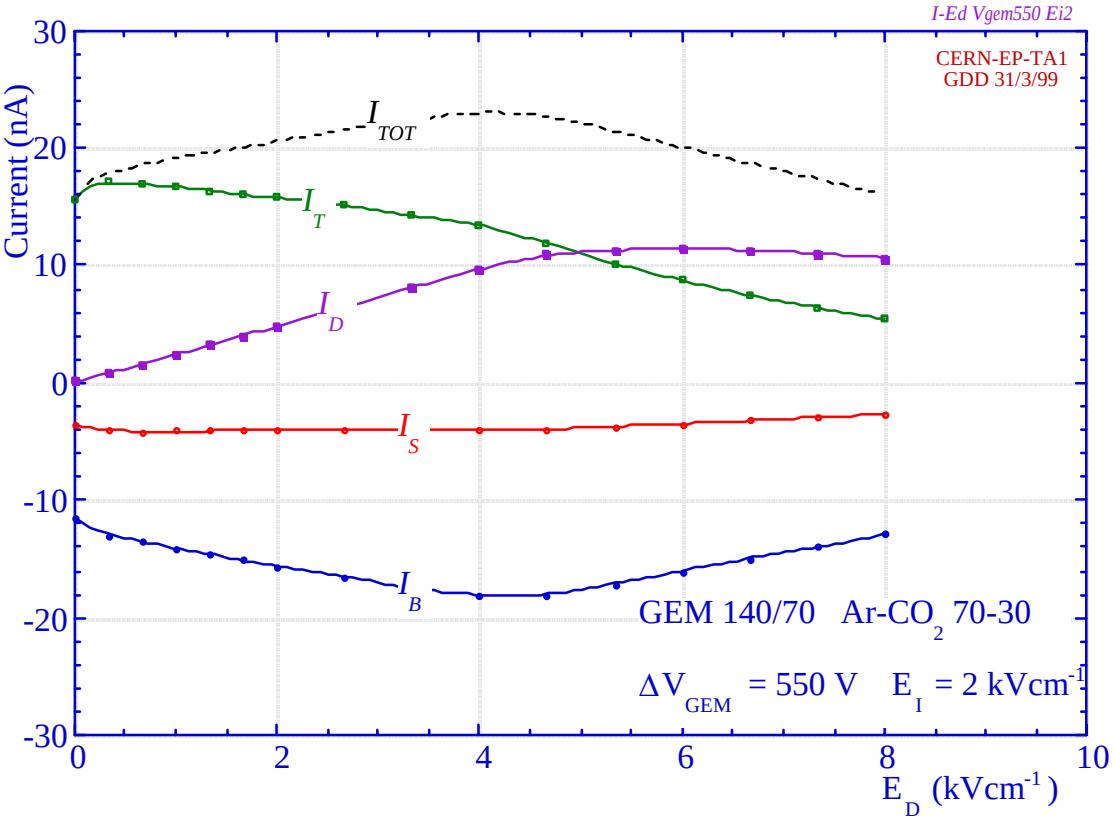

Fig. 19 (b)

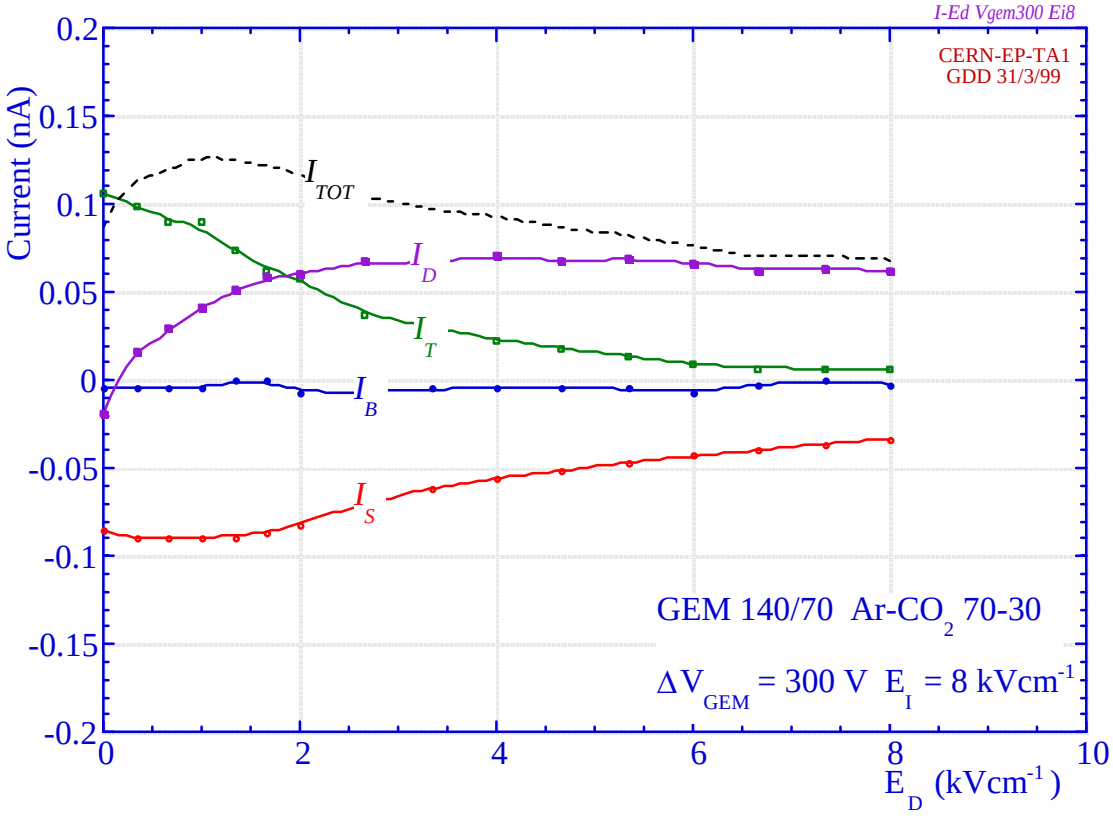

Fig. 20 (a)

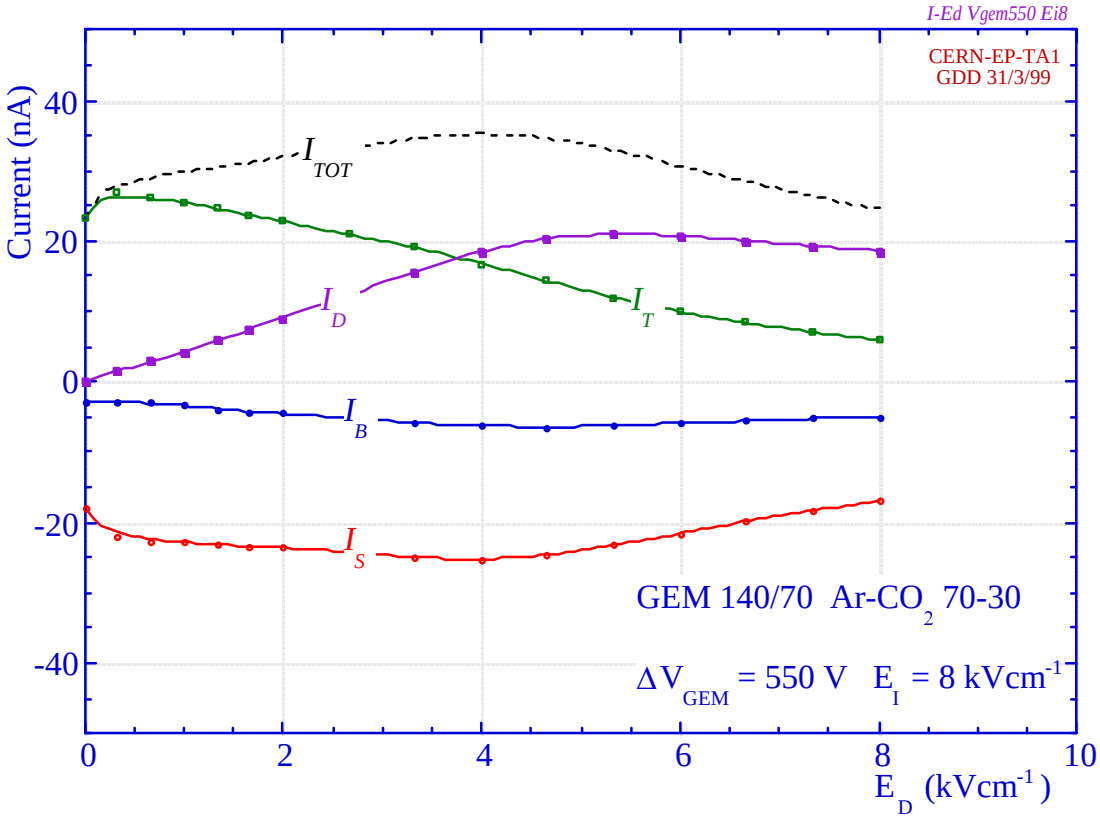

Fig. 20 (b)

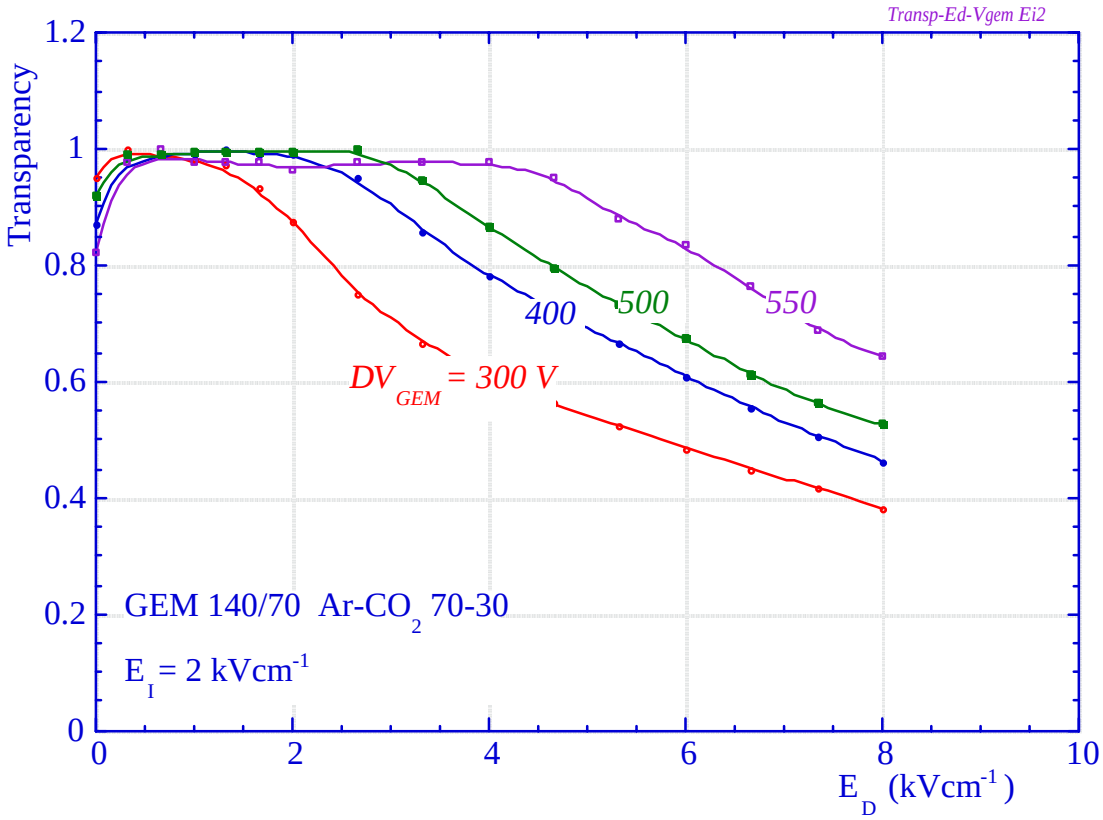

Fig. 21 (a)

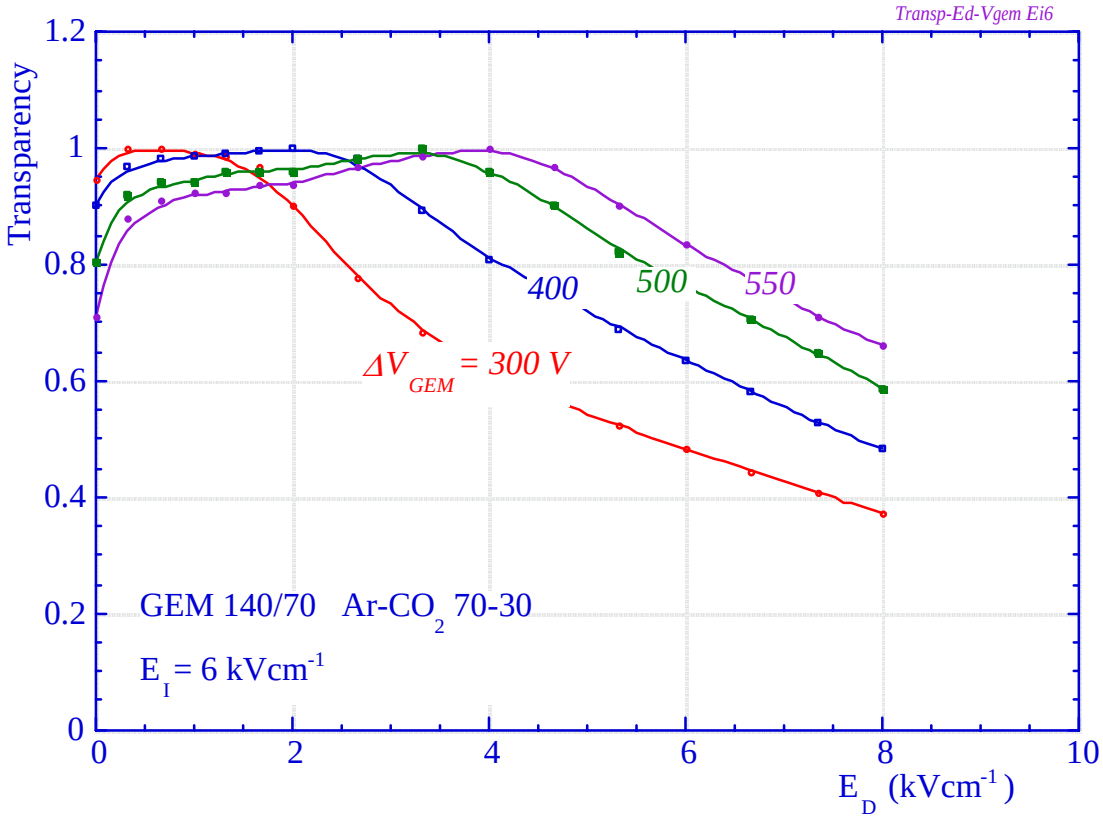

Fig. 21 (b)

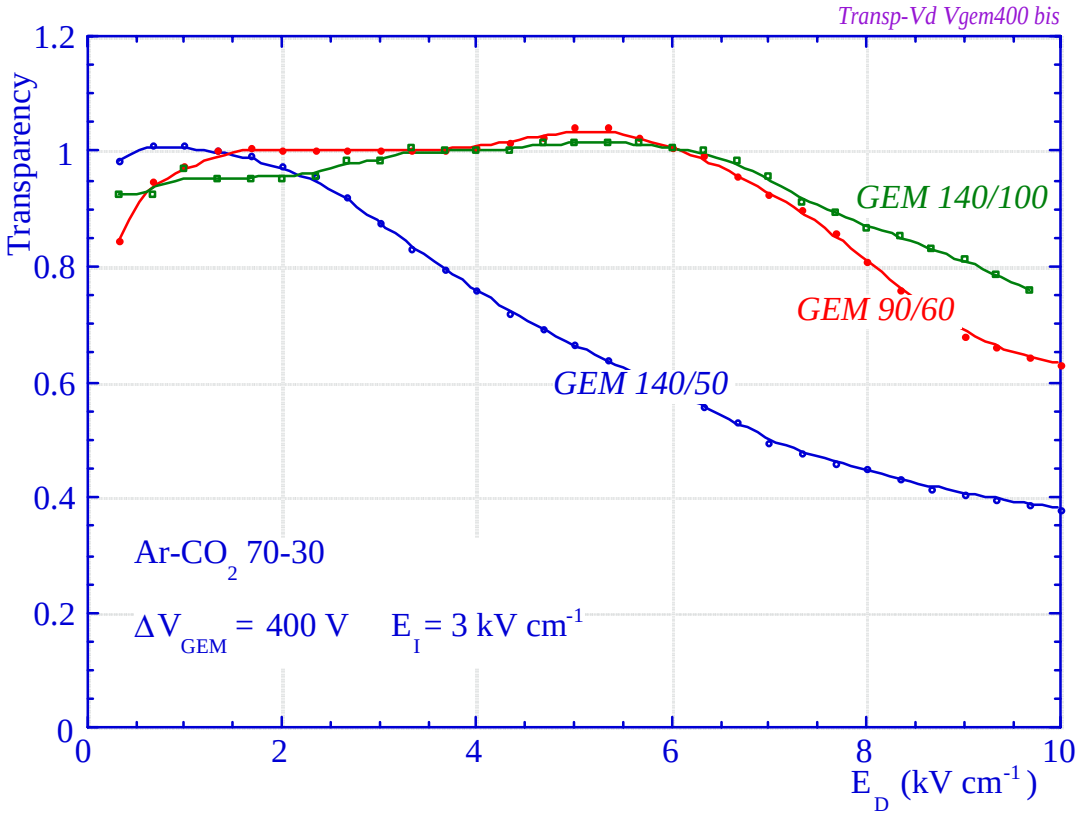

Fig. 22 (a)

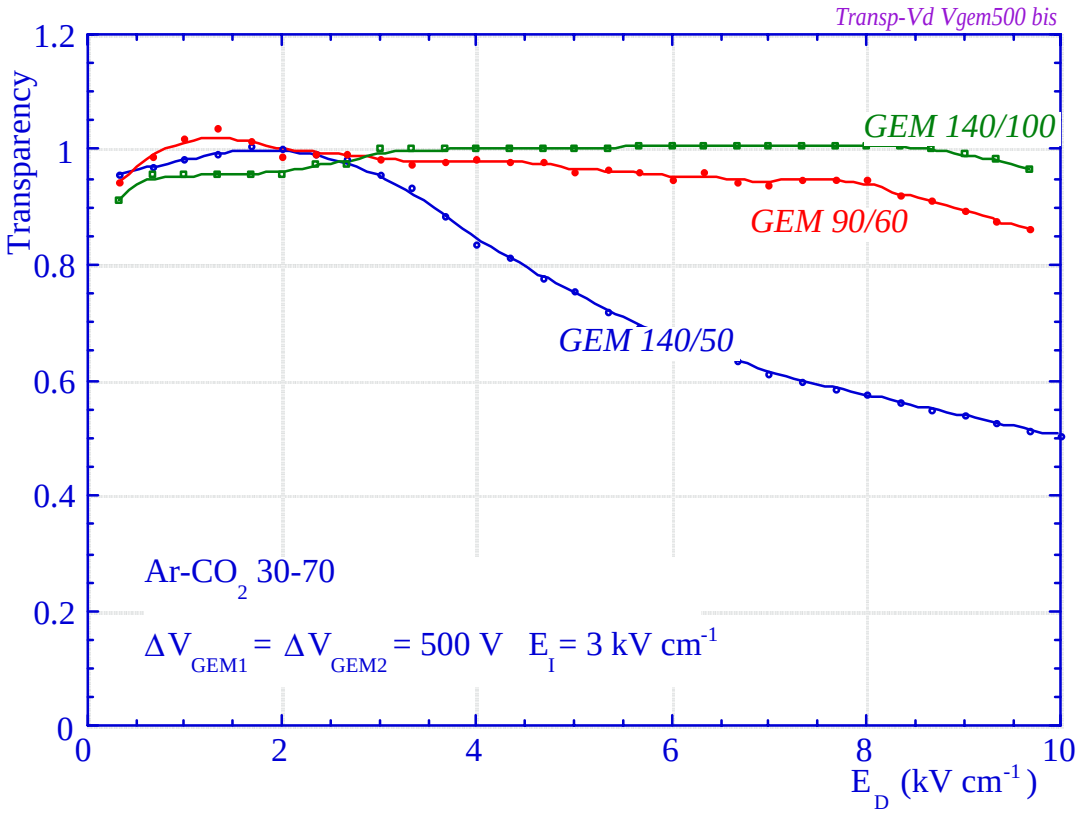

Fig. 22 (b)

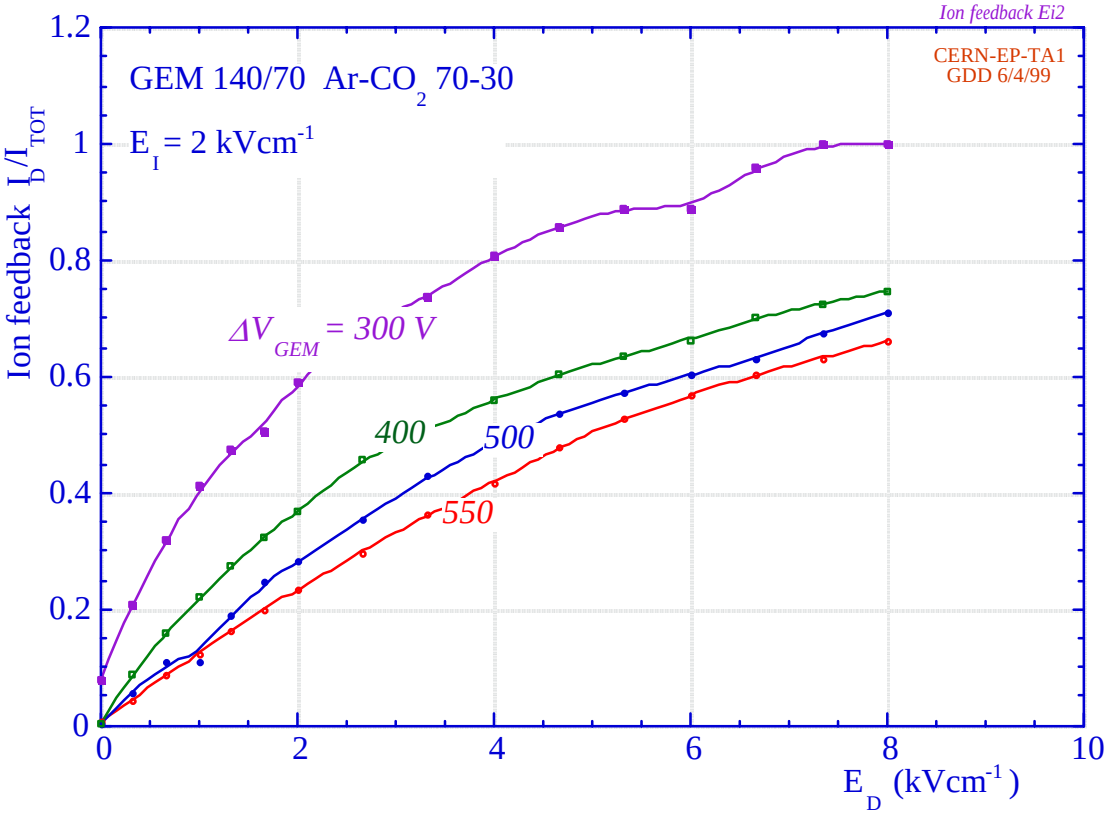

Fig. 23 (a)

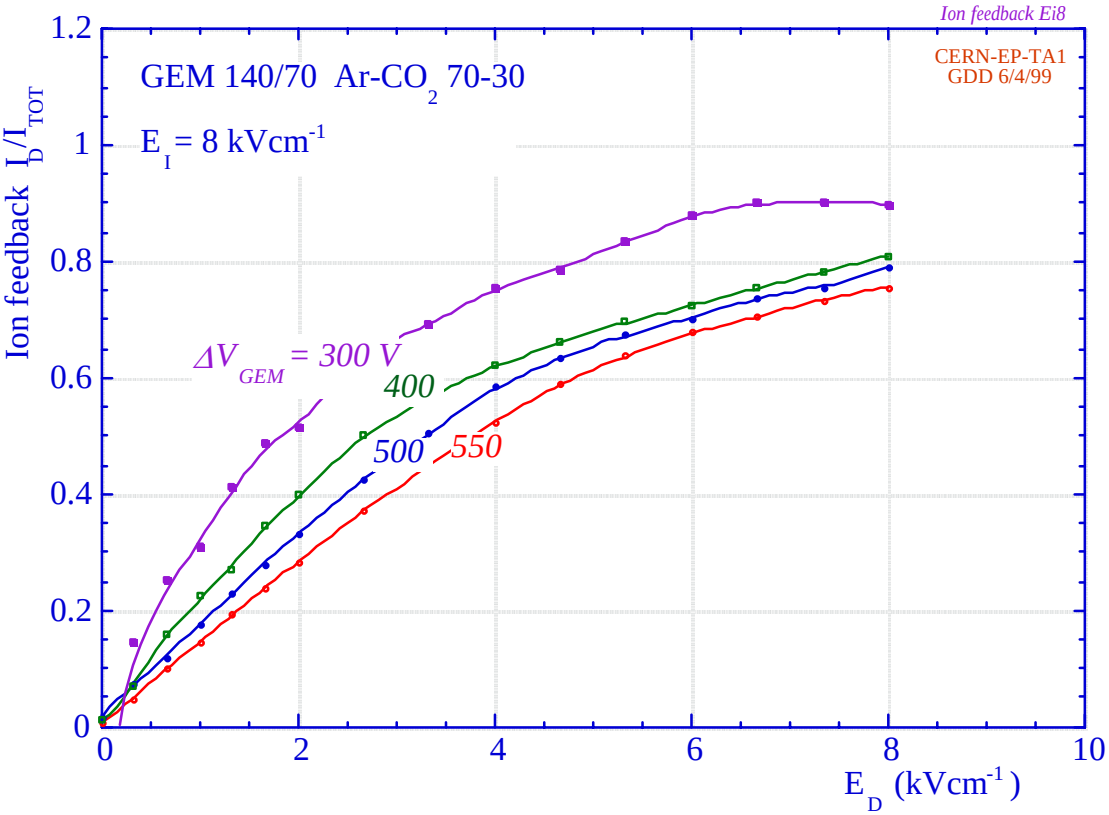

Fig. 23 (b)

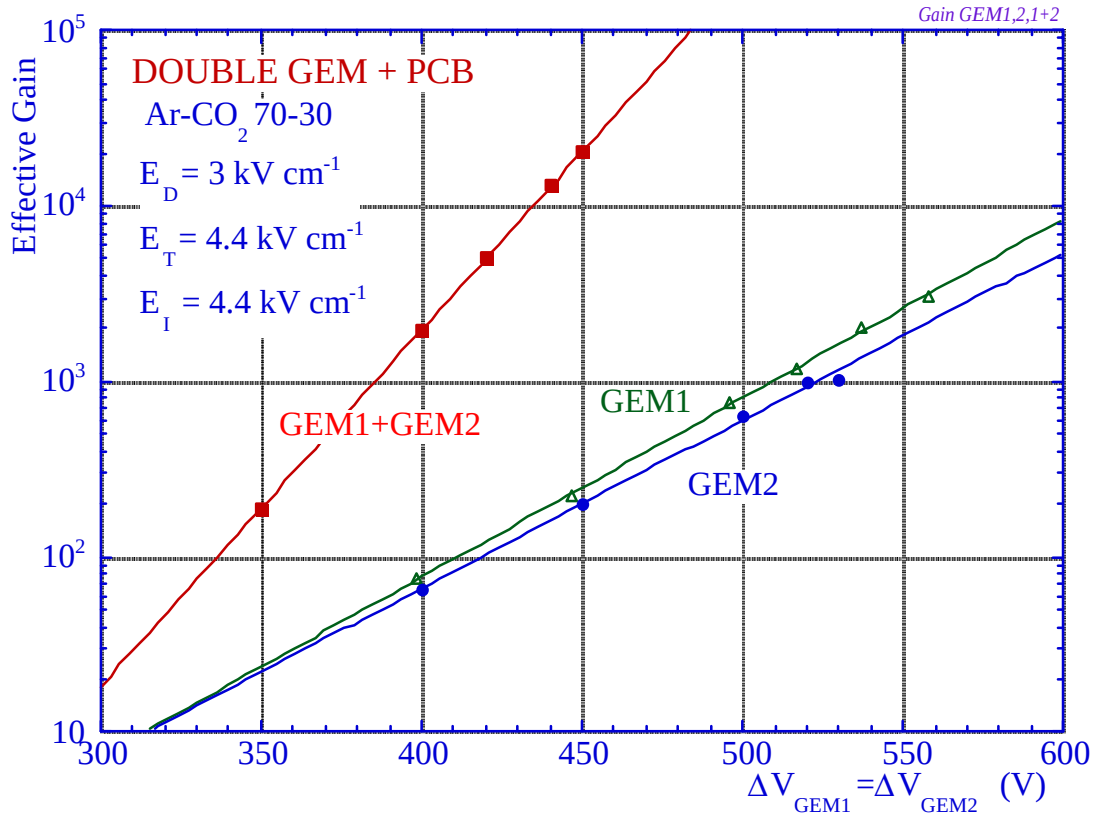
Gain GEM1,2,1+2
DOUBLE GEM + PCB
Ar-CO2 70-30
ED = 3 kV cm-1
ET = 4.4 kV cm-1
EI = 4.4 kV cm-1
GEM1+GEM2
GEM1
GEM2
Effective Gain
ΔVGEM1 =ΔVGEM2 (V)

Fig. 24

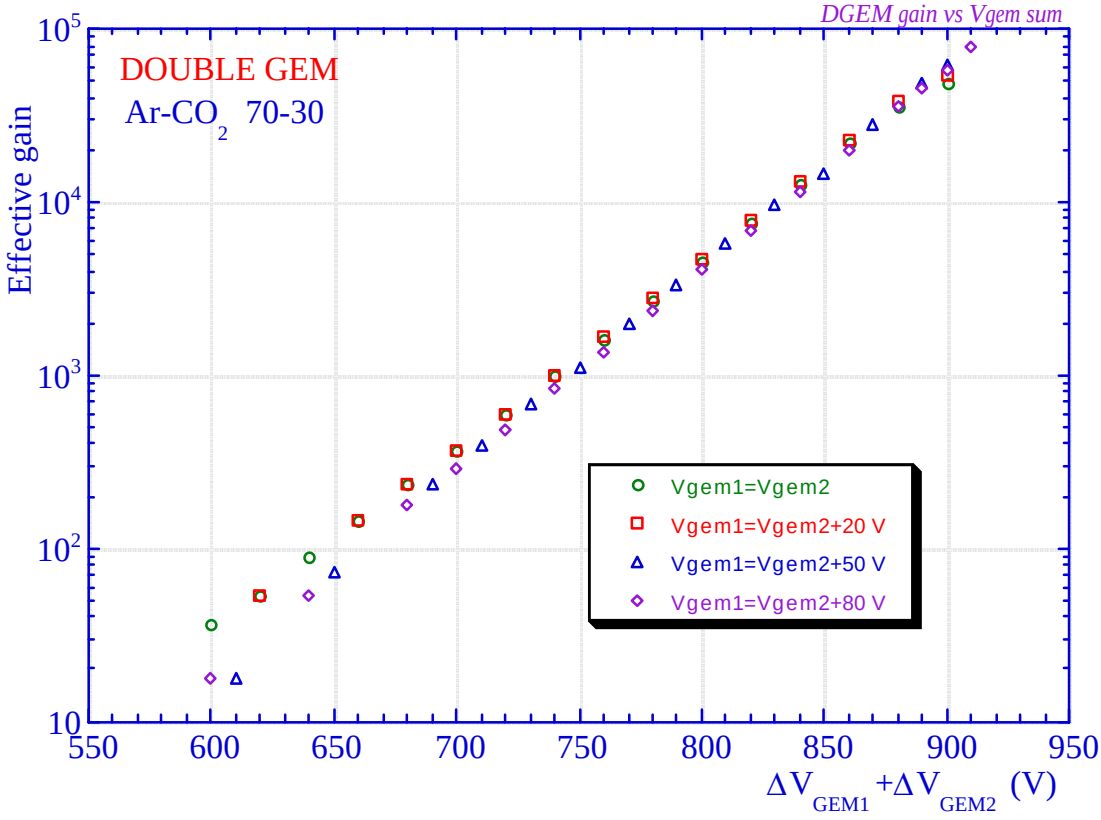
DGEM gain vs Vgem sum
DOUBLE GEM
Ar-CO2 70-30
Vgem1=Vgem2
Vgem1=Vgem2+20 V
Vgem1=Vgem2+50 V
Vgem1=Vgem2+80 V
Effective gain
ΔVGEM1 +ΔVGEM2 (V)

Fig. 25

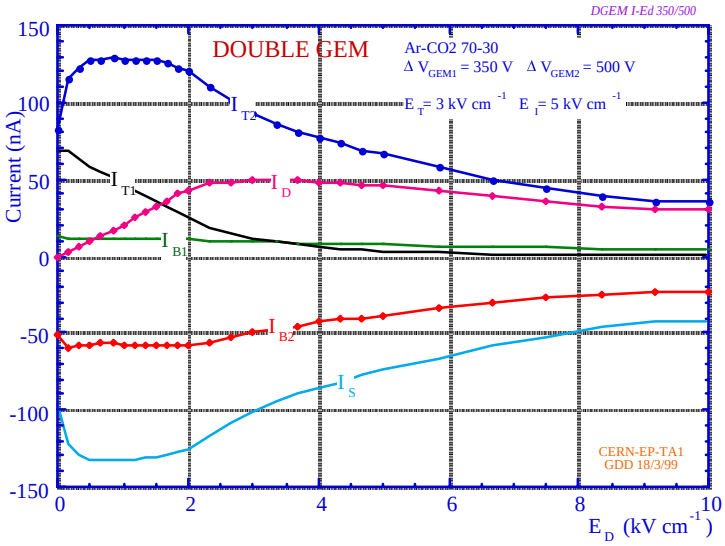

Fig. 26 (a)

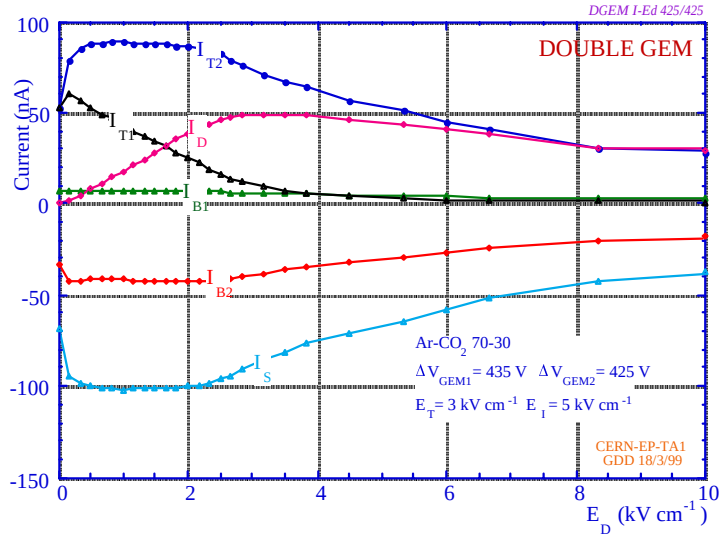

Fig. 26 (b)

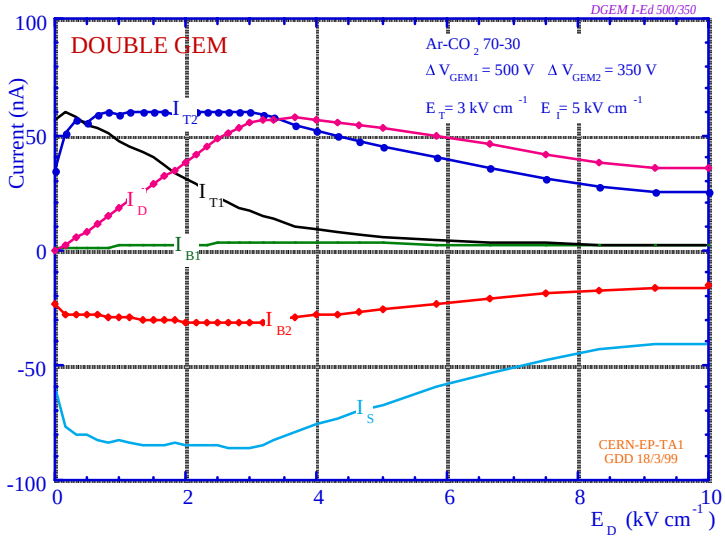

Fig. 26 (c)

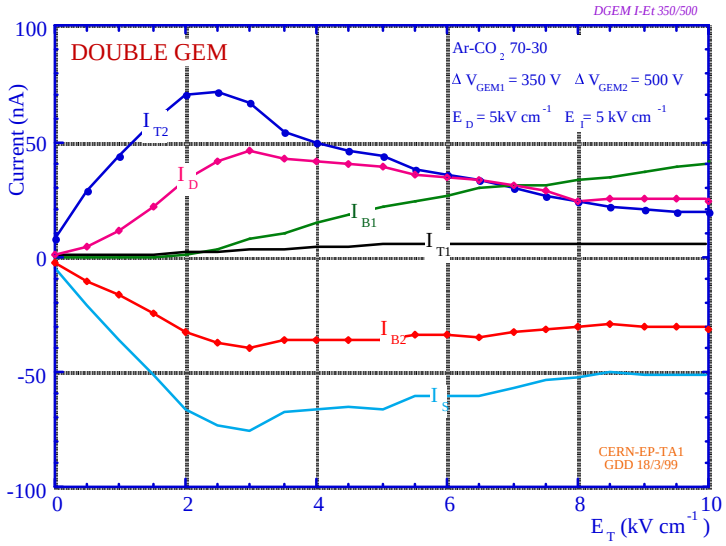

Fig. 27 (a)

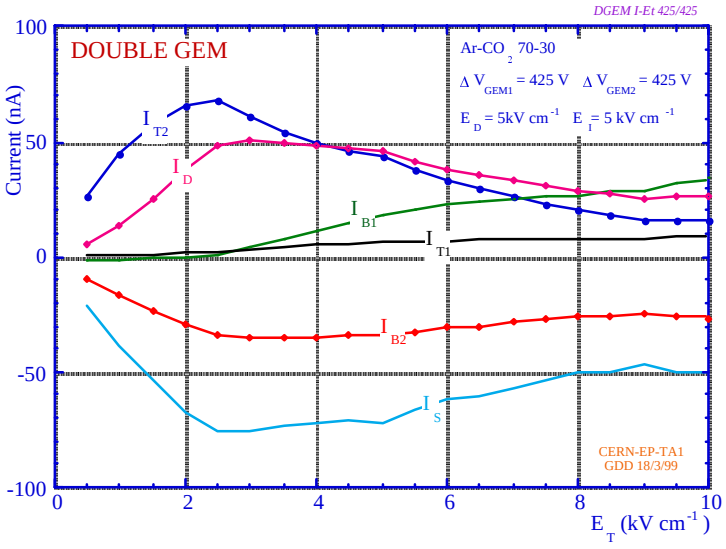

Fig. 27 (b)

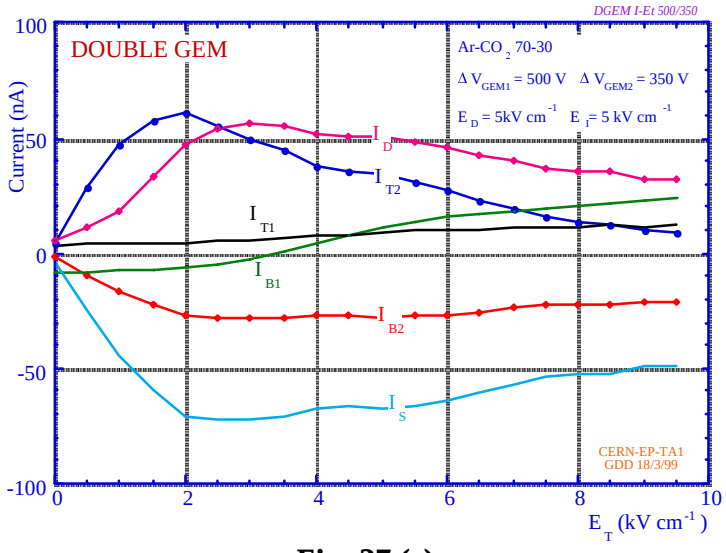

Fig. 27 (c)

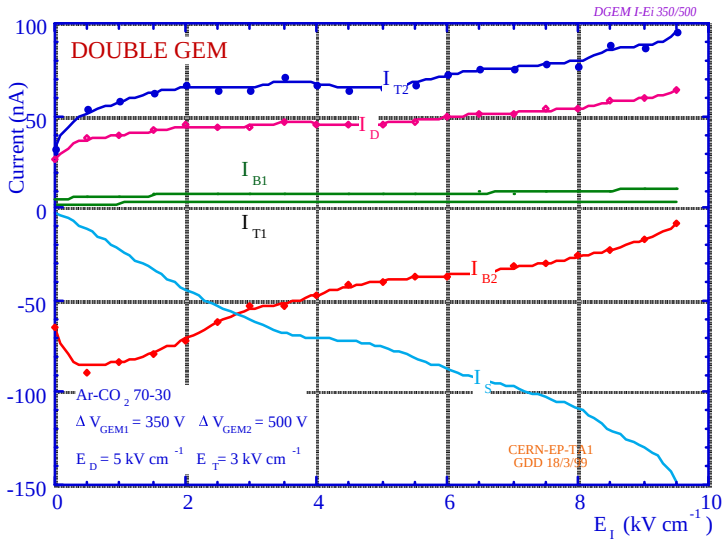

Fig. 28 (a)

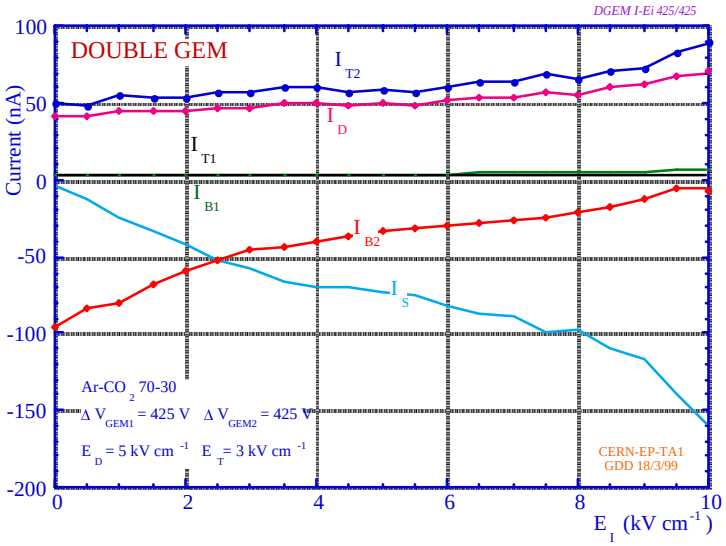

Fig. 28 (b)

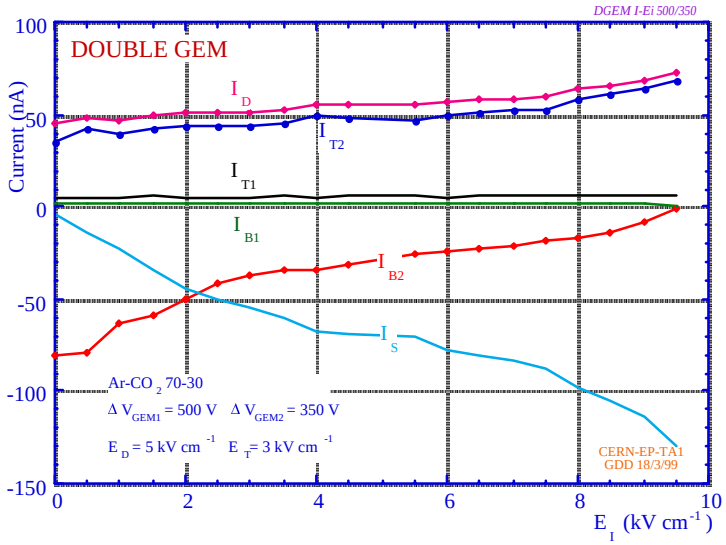

Fig. 28 (c)

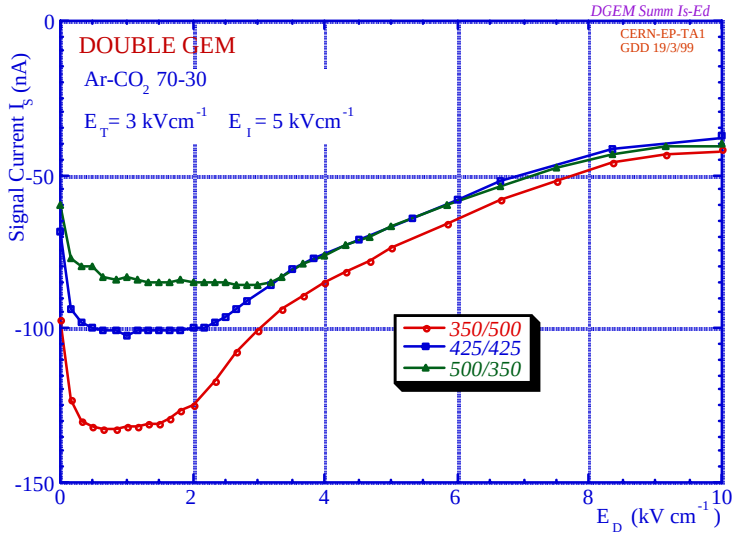

Fig. 29 (a)

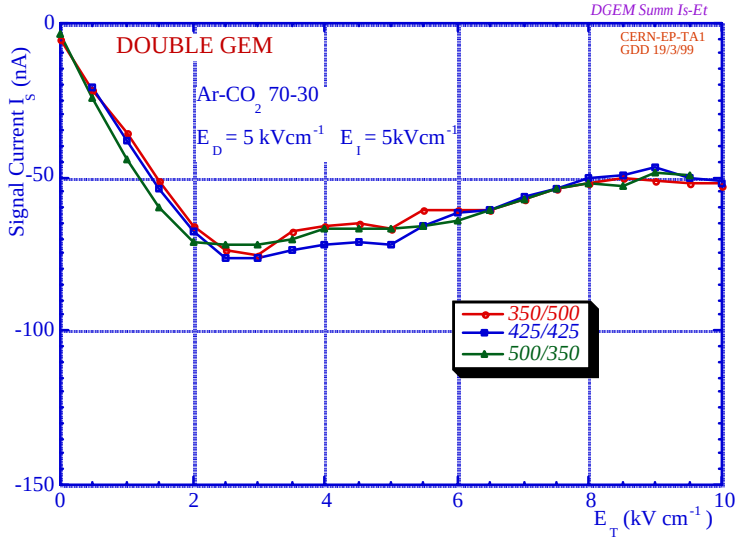

Fig. 29 (b)

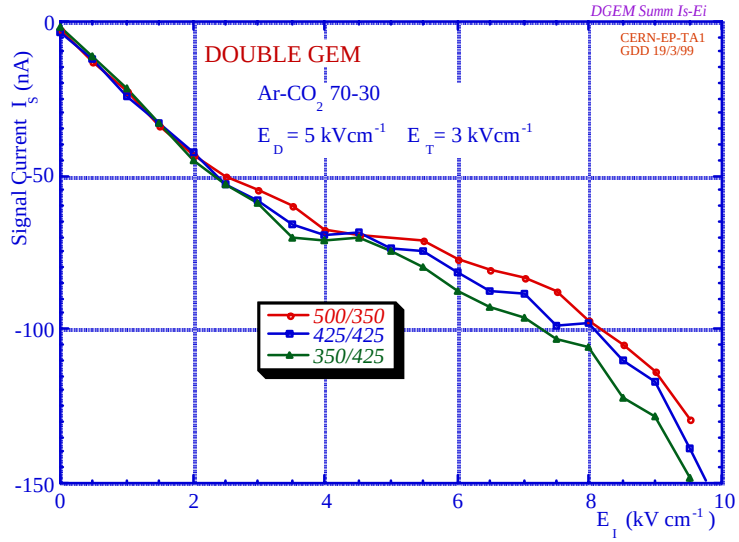

Fig. 29 (c)

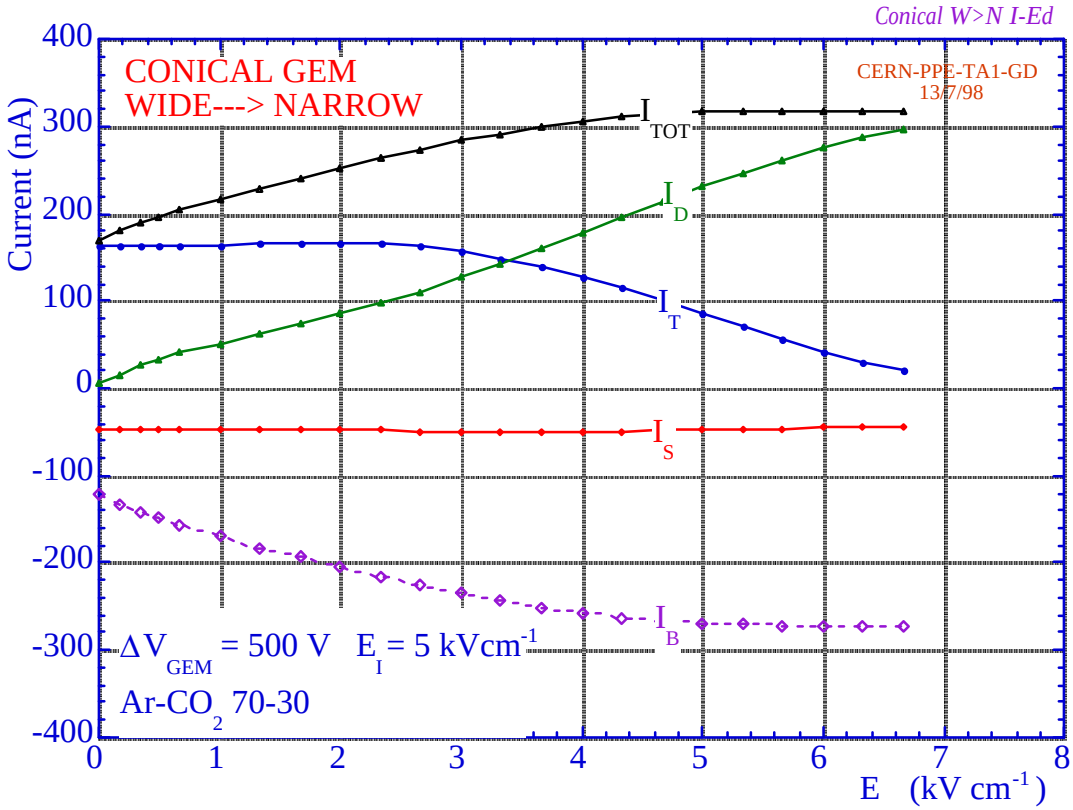

Fig. 30 (a)

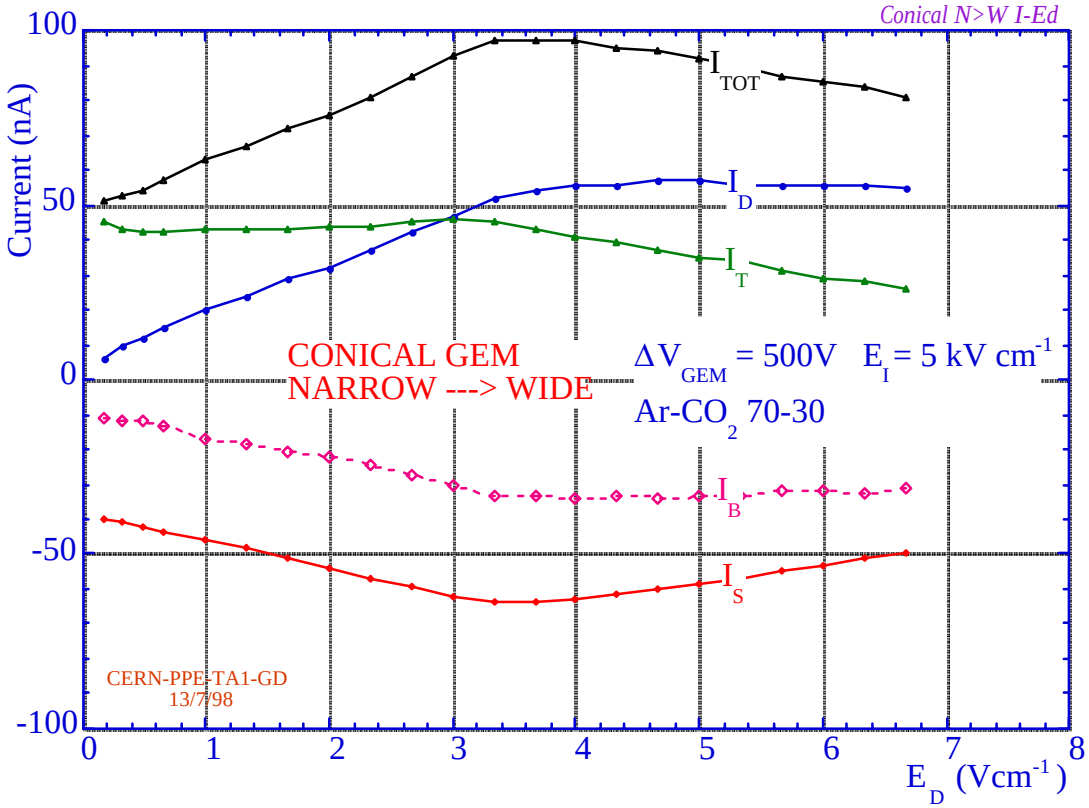

Fig. 30 (b)

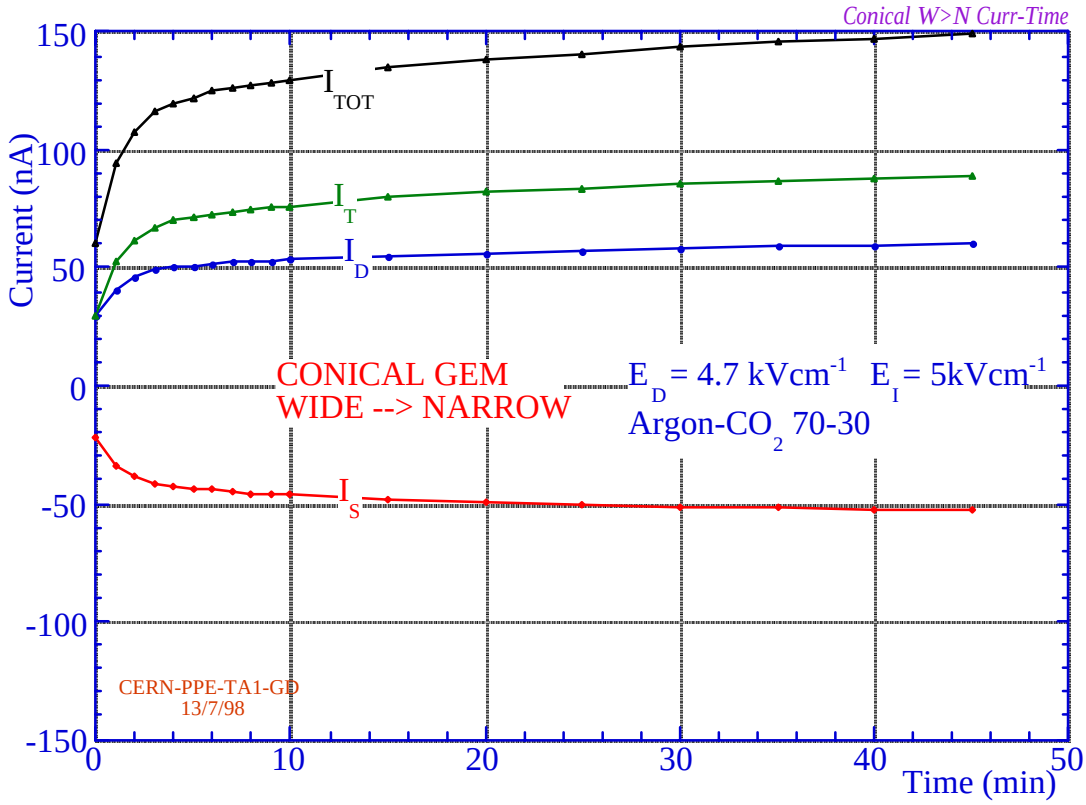

Fig. 31 (a)

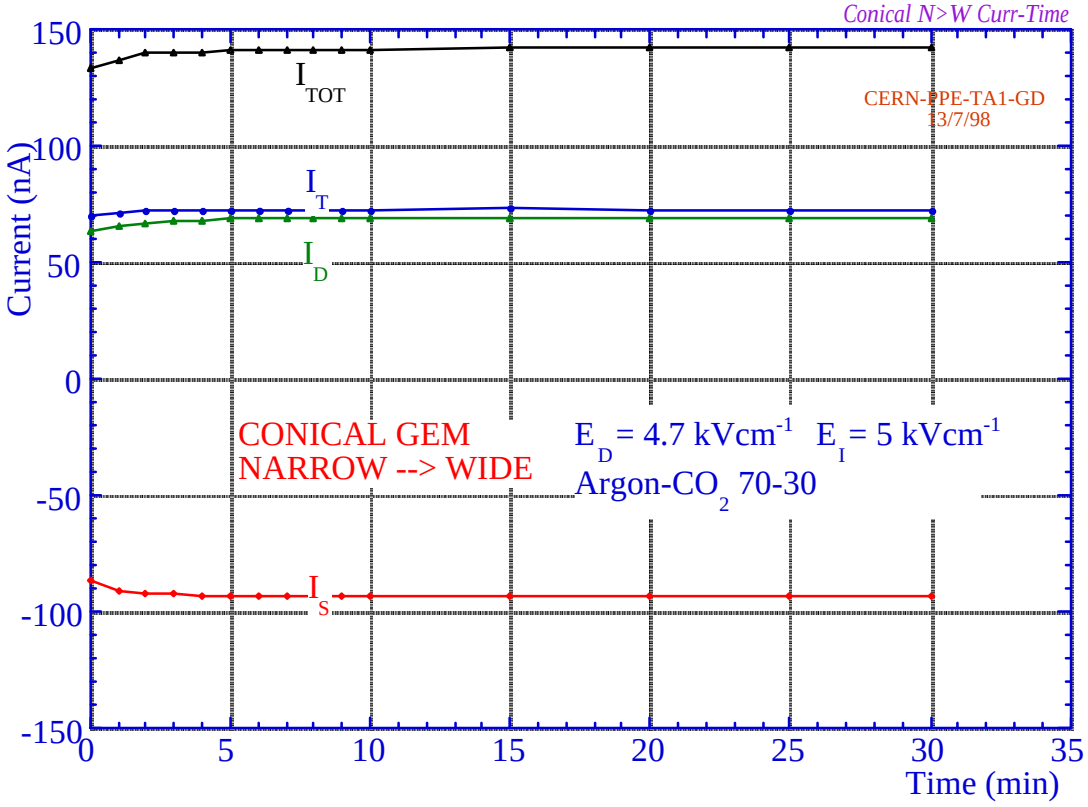

Fig. 31 (b)

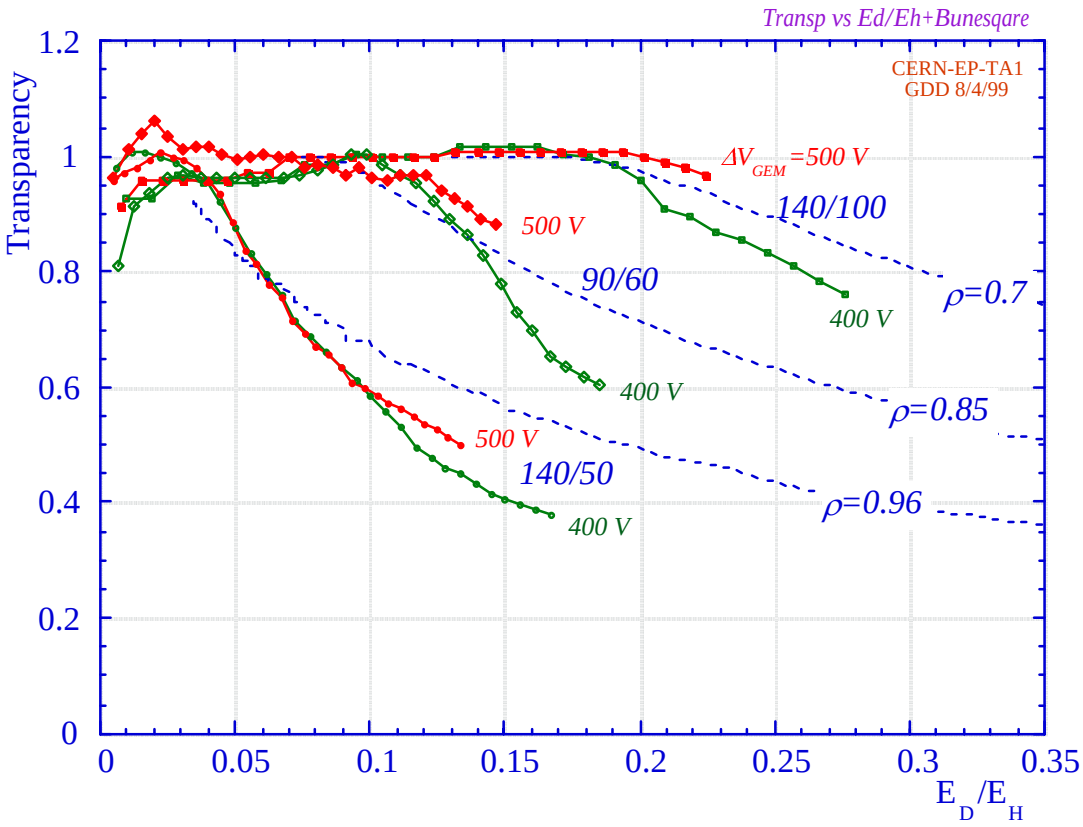
Transp vs Ed/Eh+Bunesqare
CERN-EP-TA1
GDD 8/4/99
Transparency
1.2
1
0.8
0.6
0.4
0.2
0
0
0.05
0.1
0.15
0.2
0.25
0.3
0.35
E_D/E_H
ΔV_GEM=500 V
500 V
400 V
140/100
90/60
400 V
500 V
400 V
140/50
ρ=0.7
ρ=0.85
ρ=0.96

Fig. 32

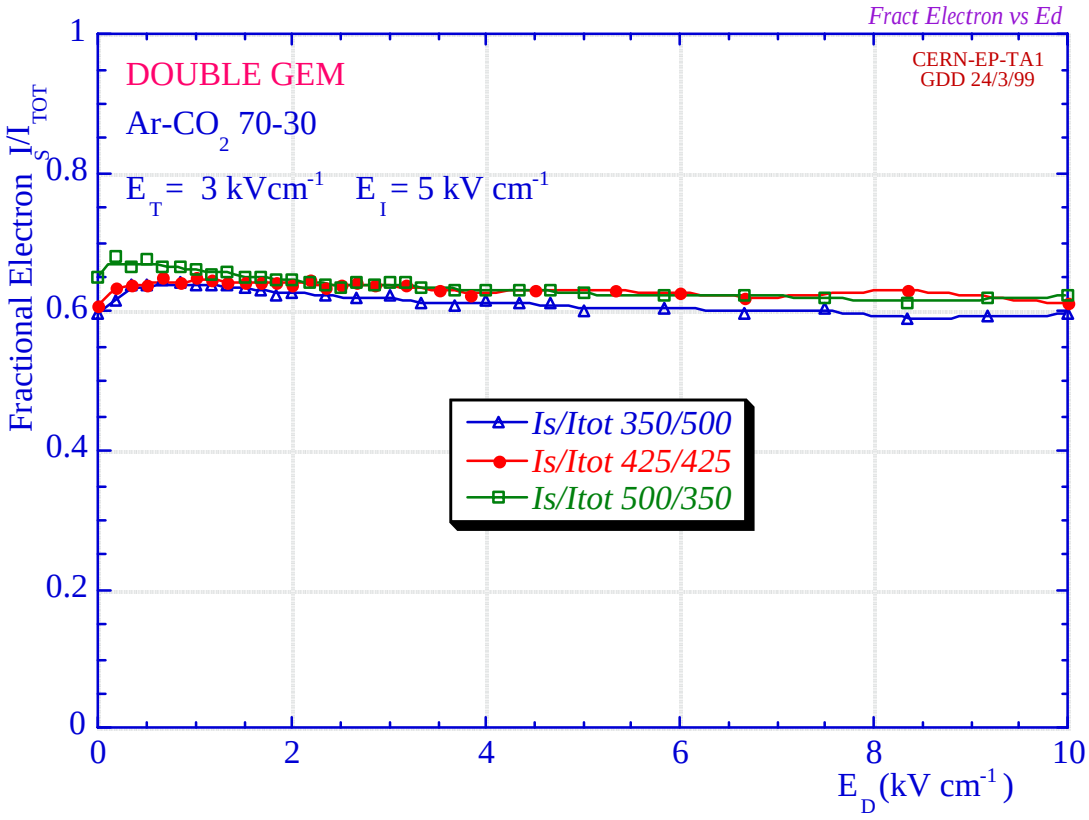
Fract Electron vs Ed
CERN-EP-TA1
GDD 24/3/99
DOUBLE GEM
Ar-CO2 70-30
E_T = 3 kVcm^-1 E_I = 5 kV cm^-1
Fractional Electron I/I_TOT
1
0.8
0.6
0.4
0.2
0
0
2
4
6
8
10
E_D (kV cm^-1)
Is/Itot 350/500
Is/Itot 425/425
Is/Itot 500/350

Fig. 33

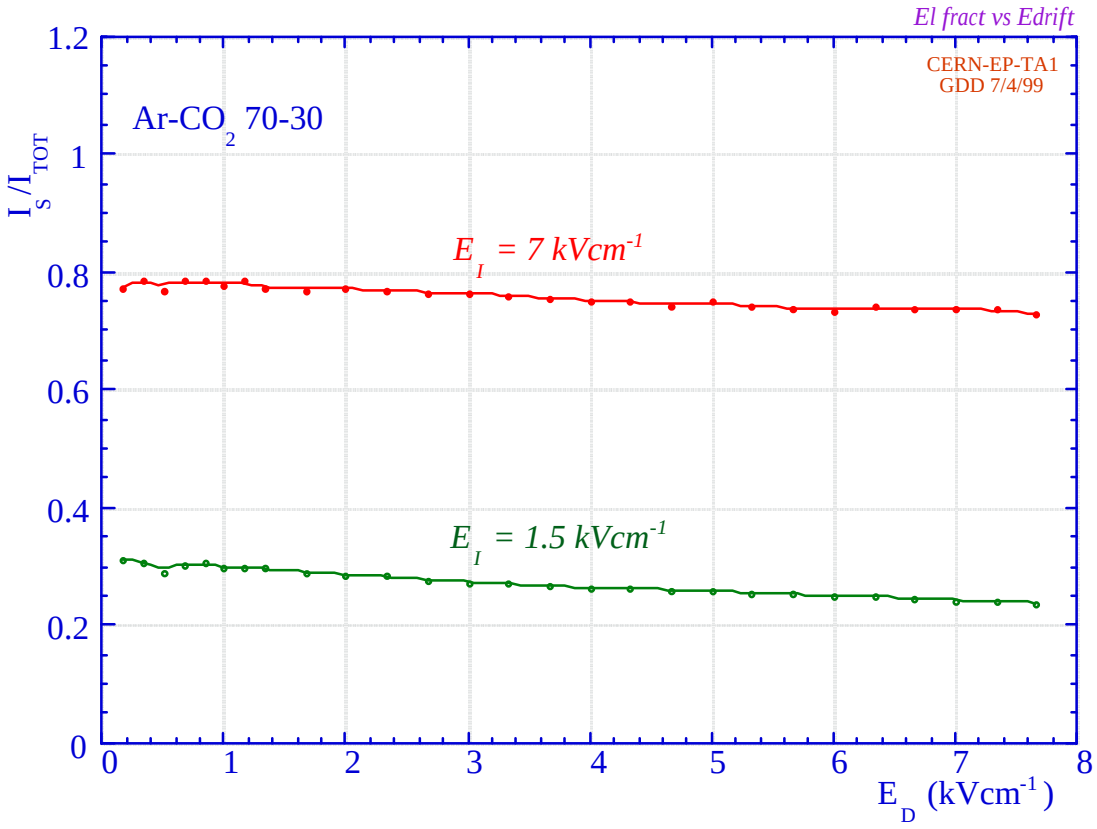
El fract vs Edrift
CERN-EP-TA1
GDD 7/4/99
Ar-CO2 70-30
E I = 7 kVcm-1
E I = 1.5 kVcm-1
I S /I TOT
E D (kVcm-1)
0
0.2
0.4
0.6
0.8
1
1.2
0
1
2
3
4
5
6
7
8

Fig. 34

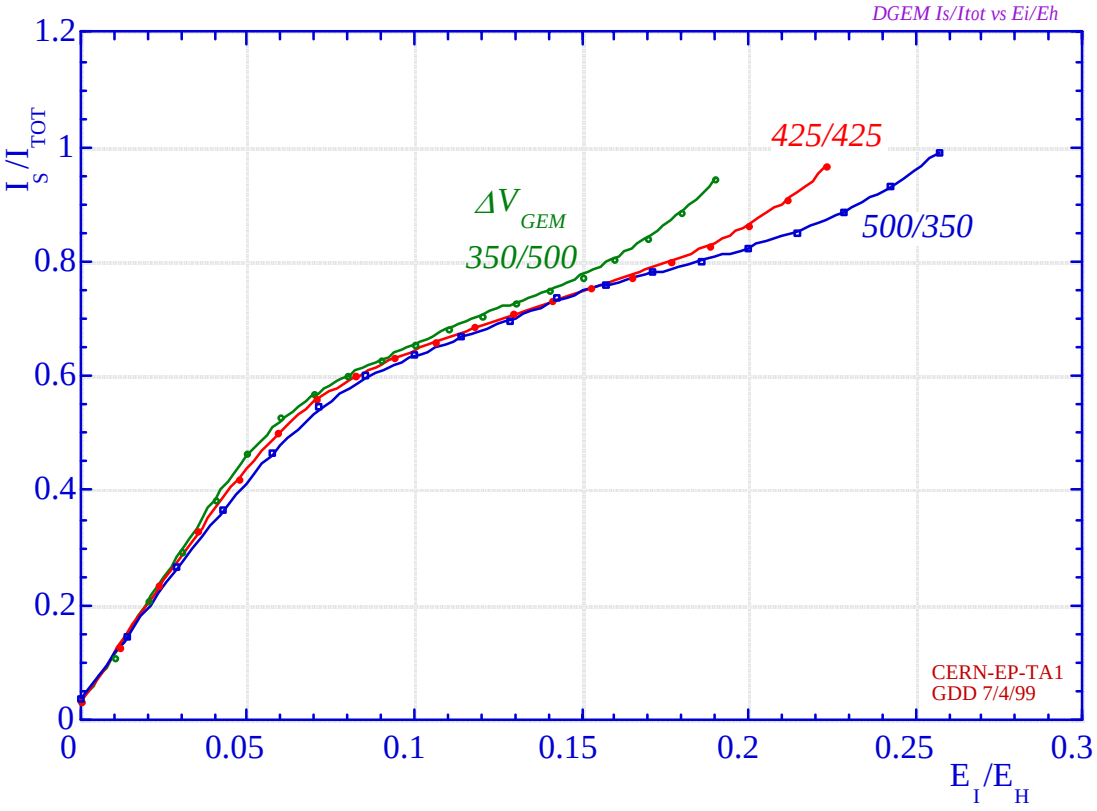
DGEM Is/Itot vs Ei/Eh
425/425
ΔV GEM
350/500
500/350
CERN-EP-TA1
GDD 7/4/99
I S /I TOT
E I /E H
0
0.2
0.4
0.6
0.8
1
1.2
0
0.05
0.1
0.15
0.2
0.25
0.3

Fig. 35

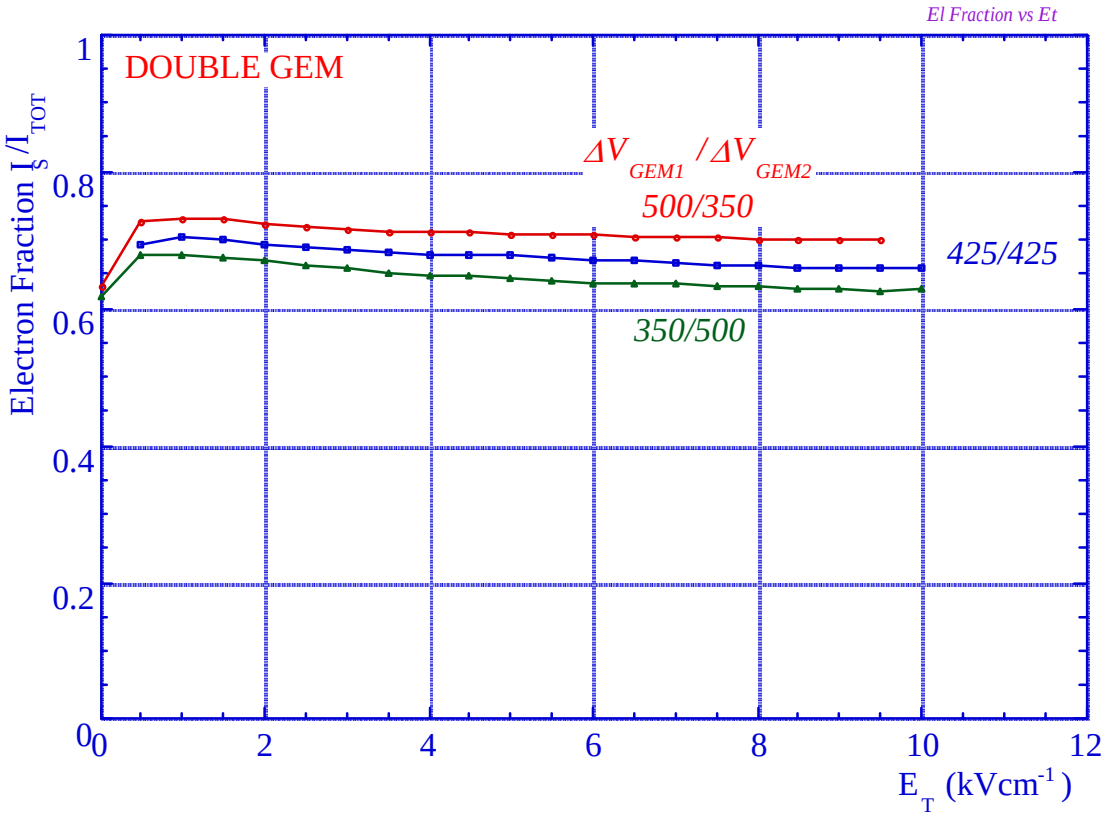
El Fraction vs Et
DOUBLE GEM
ΔV GEM1 /ΔV GEM2
500/350
425/425
350/500
Electron Fraction I_S/I_TOT
E_T (kVcm^-1)
0
0.2
0.4
0.6
0.8
1
0
2
4
6
8
10
12

Fig. 36

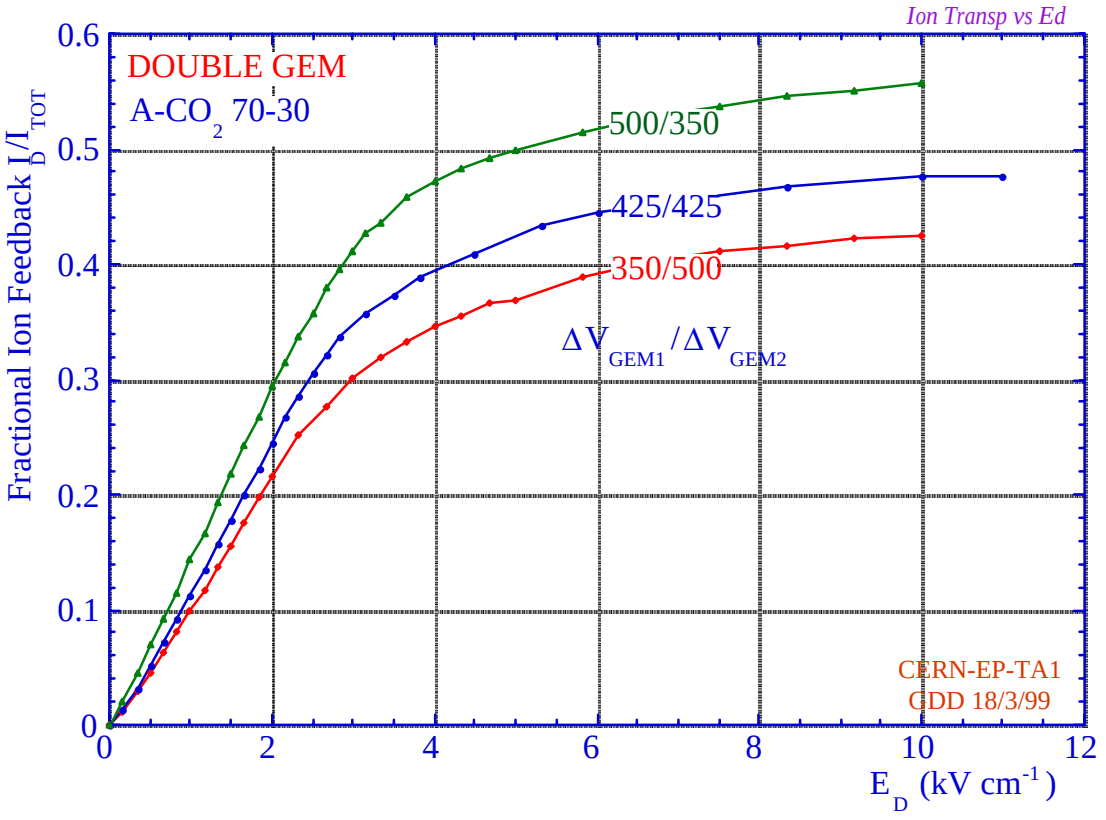
Ion Transp vs Ed
DOUBLE GEM
A-CO2 70-30
500/350
425/425
350/500
ΔV GEM1 /ΔV GEM2
CERN-EP-TA1
GDD 18/3/99
Fractional Ion Feedback I_D/I_TOT
E_D (kV cm^-1)
0
0.1
0.2
0.3
0.4
0.5
0.6
0
2
4
6
8
10
12

Fig. 37

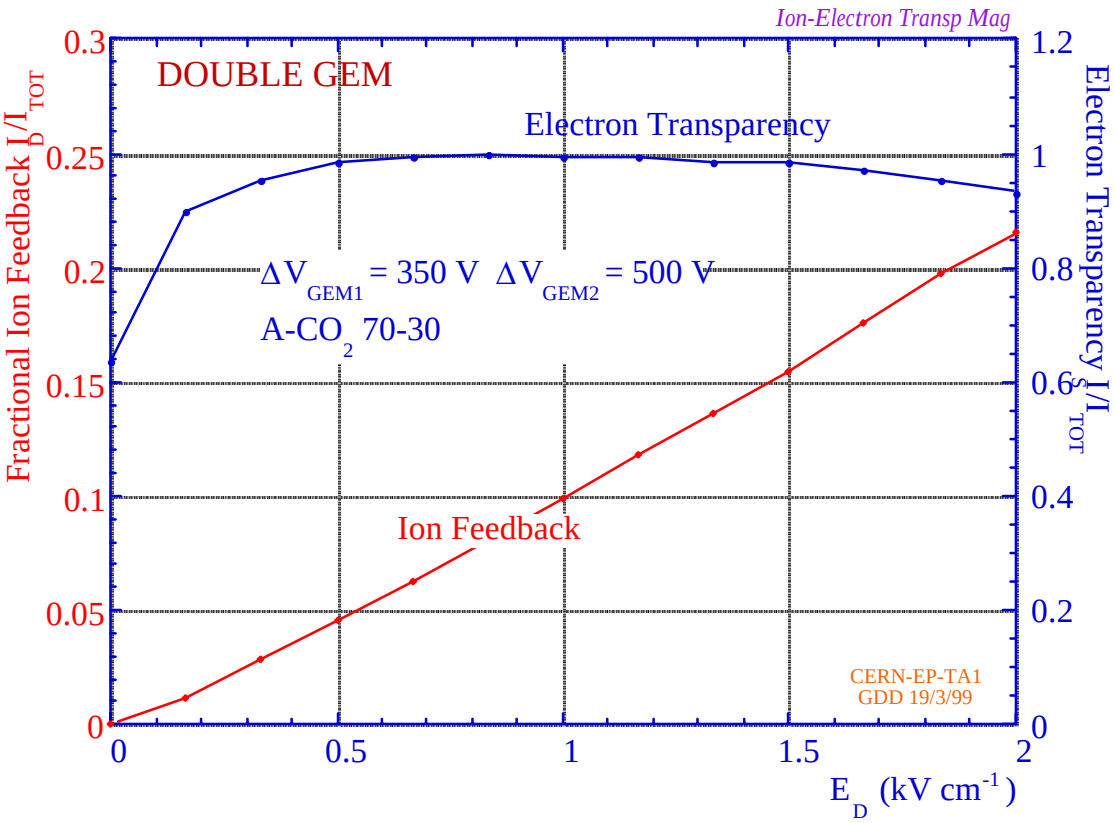
Ion-Electron Transp Mag
DOUBLE GEM
Electron Transparency
ΔV GEM1 = 350 V ΔV GEM2 = 500 V
A-CO2 70-30
Ion Feedback
CERN-EP-TA1
GDD 19/3/99
Fractional Ion Feedback I_D/I_TOT
Electron Transparency I/I_TOT
E_D (kV cm-1)
0
0.05
0.1
0.15
0.2
0.25
0.3
0.4
0.6
0.8
1
1.2
0.5
1
1.5
2

Fig. 38

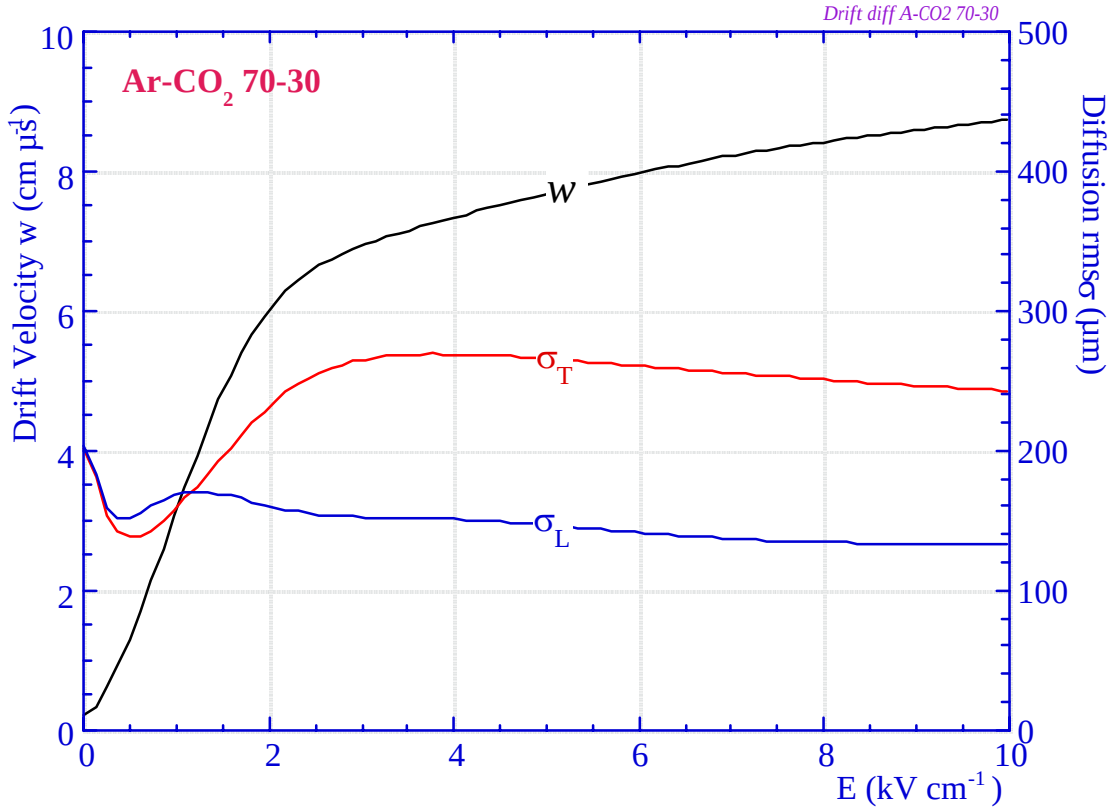
Drift diff A-CO2 70-30
Ar-CO2 70-30
w
σT
σL
Drift Velocity w (cm μs-1)
Diffusion rmsσ (μm)
E (kV cm-1)
0
2
4
6
8
10
100
200
300
400
500

Fig. A1

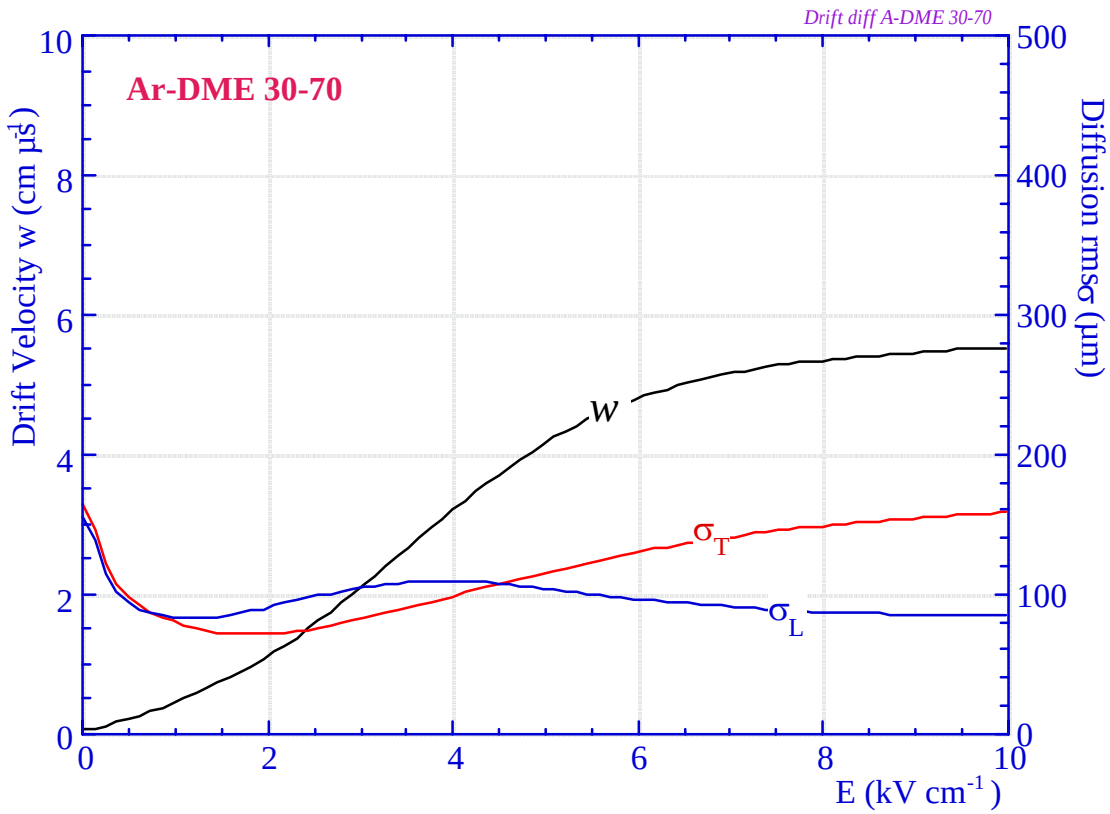
Drift diff A-DME 30-70
Ar-DME 30-70
Drift Velocity w (cm µs-1)
Diffusion rmsσ (µm)
w
σT
σL
E (kV cm-1)

Fig. A2

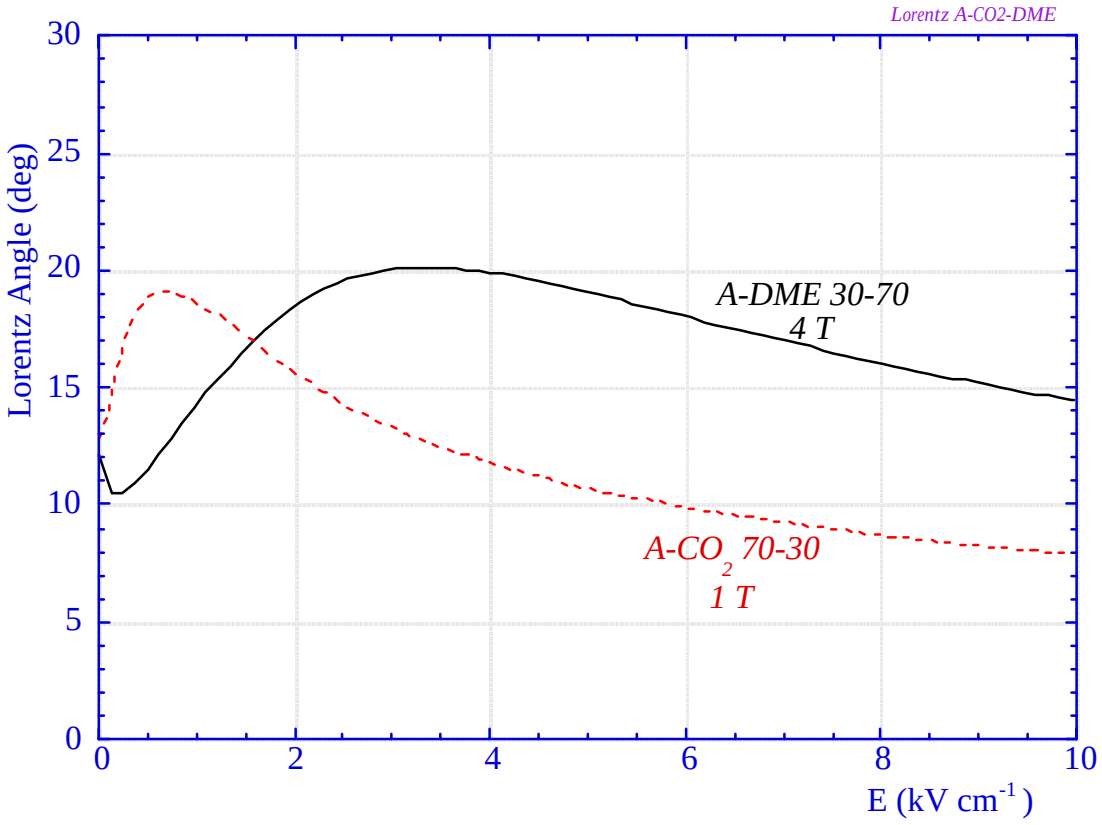
Lorentz A-CO2-DME
Lorentz Angle (deg)
A-DME 30-70
4 T
A-CO2 70-30
1 T
E (kV cm-1)

Fig. A3

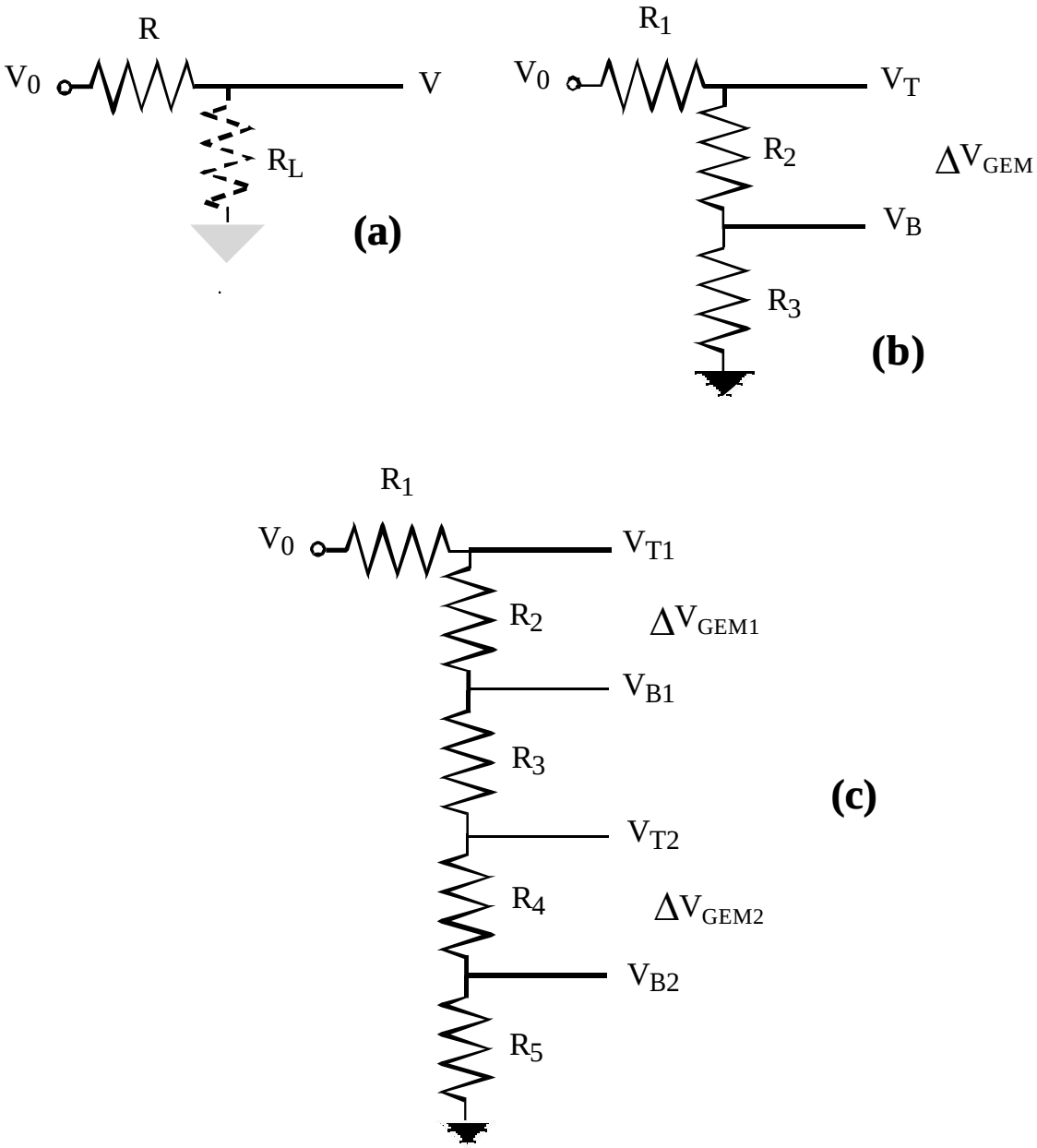
R
V0
V
RL
(a)
R1
V0
VT
R2
ΔVGEM
VB
R3
(b)
R1
V0
VT1
R2
ΔVGEM1
VB1
R3
(c)
VT2
R4
ΔVGEM2
VB2
R5

Fig. A4